

University of Massachusetts Medical School

eScholarship@UMMS

University of Massachusetts Medical School Faculty Publications

2019-10-10

FMRP Control of Ribosome Translocation Promotes Chromatin Modifications and Alternative Splicing of Neuronal Genes Linked to Autism


Sneha Shah

University of Massachusetts Medical School

Et al.

Let us know how access to this document benefits you.

Follow this and additional works at: https://escholarship.umassmed.edu/faculty_pubs

 Part of the [Amino Acids, Peptides, and Proteins Commons](#), [Congenital, Hereditary, and Neonatal Diseases and Abnormalities Commons](#), [Genetic Phenomena Commons](#), [Mental Disorders Commons](#), [Nervous System Diseases Commons](#), [Neuroscience and Neurobiology Commons](#), and the [Nucleic Acids, Nucleotides, and Nucleosides Commons](#)

Repository Citation

Shah S, Molinaro G, Liu B, Wang R, Huber KM, Richter JD. (2019). FMRP Control of Ribosome Translocation Promotes Chromatin Modifications and Alternative Splicing of Neuronal Genes Linked to Autism. University of Massachusetts Medical School Faculty Publications. <https://doi.org/10.1101/801076>. Retrieved from https://escholarship.umassmed.edu/faculty_pubs/1642

Creative Commons License



This work is licensed under a [Creative Commons Attribution-Noncommercial-No Derivative Works 4.0 License](#). This material is brought to you by eScholarship@UMMS. It has been accepted for inclusion in University of Massachusetts Medical School Faculty Publications by an authorized administrator of eScholarship@UMMS. For more information, please contact Lisa.Palmer@umassmed.edu.

1 **FMRP Control of Ribosome Translocation Promotes Chromatin Modifications and**
2 **Alternative Splicing of Neuronal Genes Linked to Autism**

3
4
5 Sneha Shah^{1,3} Gemma Molinaro^{2,3}, Botao Liu^{1,3}, Ruijia Wang¹, Kimberly M. Huber^{2,4}, and Joel D.
6 Richter^{1,4}

7
8 ¹Program in Molecular Medicine

9 University of Massachusetts Medical School

10 Worcester, MA 01605

11
12 ²Department of Neuroscience

13 University of Texas Southwestern Medical School

14 Dallas, TX 75390

15
16 ³equal contributors

17
18 ⁴corresponding authors: kimberly.huber@utsouthwestern.edu (K.M.H.),
19 joel.richter@umassmed.edu (J.D.R.)
20
21

1 **Abstract**

2 Silencing of *FMR1* and loss of its gene product FMRP results in Fragile X Syndrome. FMRP binds
3 brain mRNAs and inhibits polypeptide elongation. Using ribosome profiling of the hippocampus,
4 we find that ribosome footprint levels in *Fmr1*-deficient tissue mostly reflect changes in RNA
5 abundance. Profiling over a time course of ribosome runoff in wildtype tissue reveals a wide range
6 of ribosome translocation rates; on many mRNAs, the ribosomes are stalled. Sucrose gradient
7 ultracentrifugation of hippocampal slices after ribosome runoff reveals that FMRP co-sediments
8 with stalled ribosomes; and its loss results in decline of ribosome stalling on specific mRNAs. One
9 such mRNA encodes SETD2, a lysine methyltransferase that catalyzes H3K36me3. ChIP-Seq
10 demonstrates that loss of FMRP alters the deployment of this epigenetic mark on chromatin.
11 H3K36me3 is associated with alternative pre-RNA processing, which we find occurs in an FMRP-
12 dependent manner on transcripts linked to neural function and autism spectrum disorders.

13

Introduction

1
2
3
4
5
6
7
8
9
10
11
12
13
14
15
16
17
18
19
20
21
22
23
24
25
26

The Fragile Syndrome (FXS) is characterized by intellectual disability, developmental delays, social impairment, hyper-anxiety, and other maladies. The root cause of FXS is an iteration of ~200 or more CGG triplets in *FMR1* that induces DNA methylation and transcriptional inactivation. Loss of the *FMR1* gene product FMRP results in synaptic dysfunction and aberrant circuit formation, which produces neuro-pathological conditions during development (Santoro et al 2012). FXS is modeled in *Fmr1* knockout mice, which mimic many facets of the human disease including learning and memory deficits, repetitive disorders, susceptibility to seizures, etc. In these animals, neuronal communication is frequently examined at hippocampal Schaffer collateral-CA1 synapses, which exhibit exaggerated metabotropic glutamate receptor-dependent long term depression (mGluR-LTD) (Huber et al 2002). This form of synaptic plasticity normally requires protein synthesis but in *Fmr1*-deficient animals, protein synthesis is both unnecessary for mGluR-LTD and excessive in neurons, which contributes to aberrant circuit formation and other hallmarks of the syndrome (Waung and Huber 2009).

FMRP is an RNA binding protein present in most cells; in neurons, its localization at postsynaptic sites is thought to control activity-dependent synapse remodeling by regulating mRNA expression (Richter et al 2015). Considerable effort has been made to identify FMRP target mRNAs but the most rigorous involves *in vivo* crosslink and immunoprecipitation (CLIP). CLIP combined with RNA-seq has identified 842 target mRNAs in the p11-p25 mouse cortex and cerebellum (Darnell et al 2011), predominantly a single mRNA in cultured cortical neurons (Tabet et al 2016), 1610 RNAs in the p13 cortex, hippocampus, and cerebellum (Maurin et al 2018), and ~6000 RNAs in HEK cells ectopically expressing epitope-tagged FMRP (Ascano et al 2012). This diversity of FMRP CLIP targets could reflect the different procedures employed or the different brain cell types examined. Surprisingly, the majority of CLIP sites in mRNA are in coding regions (Darnell et al 2011; Maurin et al 2018), with perhaps a bias to some cis sequences (Anderson et

1 al 2016; Maurin et al 2018). FMRP association with mRNA coding regions and co-sedimentation
2 with polyribosomes in sucrose gradients (Khandjian et al 1996; Feng et al 1997; Stefani et al
3 2004) suggests that it normally inhibits translation by impeding ribosome translocation. Indeed,
4 studies that examined polypeptide elongation directly (Udagawa et al 2013) or susceptibility to
5 puromycin release of nascent polypeptides (Darnell et al 2011) indicate that FMRP regulates
6 translation at the level of ribosome transit. Supporting evidence comes from studies showing that
7 *Drosophila* FMRP interacts with ribosomal protein L5 (rpL5) (Ishizuka et al 2002), which may
8 preclude tRNA or elongation factors from engaging the ribosome, thereby leading to a stalled
9 configuration (Chen et al 2014). Although these observations need to be extended to mammalian
10 FMRP, they suggest a molecular mechanism by which FMRP stalls ribosomes. However, such
11 observations do not indicate whether or how FMRP could stall ribosomes on specific mRNAs.

12 Ribosome profiling is a whole genome method for analyzing the number and positions of
13 ribosomes associated with mRNA; when combined with RNA-seq, it yields valuable and
14 heretofore unobtainable information on gene expression at high resolution (Ingolia et al 2009;
15 Ingolia 2014; Brar and Weismann 2015). We have used this method to explore FMRP regulation
16 of gene expression in mouse adult neural stems cells (aNSCs), which in FXS have an abnormal
17 proclivity to differentiate into glia at the expense of neurons (Luo et al 2010; Guo 2011). We
18 identified hundreds of mRNAs whose ribosome occupancy was up or down regulated in FMRP-
19 deficient cells, demonstrated that hundreds of other mRNAs had altered steady state levels and
20 whose ribosome association reflected these alterations, and discovered yet additional mRNAs
21 whose ribosome occupancy was “buffered” so that changes in their levels was compensated for
22 by opposite changes in ribosome association (Liu et al 2018).

23 Ribosome profiling at steady state cannot distinguish between translocating and stalled
24 ribosomes, suggesting that studies examining FMRP-regulated translation by this method or ribo-
25 TRAP (Thomson et al 2017; Liu et al 2018, 2019; Greenblatt and Spradling 2018; Das Sharma et
26 al 2019) may overlook key events leading to FXS. Moreover, if intact brain circuitry is important

1 for FMRP regulation, then culturing disaggregated neurons, for example, might not reveal
2 important aspects of FMRP function. To circumvent these issues, we have developed a
3 hippocampal slice assay to detect mRNA-specific ribosome translocation dynamics. Hippocampal
4 slices maintain the in vivo synaptic connectivity and cellular architecture, as well as express
5 protein synthesis and FMRP-dependent forms of synaptic plasticity (Huber et al., 2002). Profiling
6 over a time course of ribosome runoff in slices demonstrates a wide range of ribosome
7 translocation rates on specific mRNAs, ranging from rapid (rates similar to those in ES cells,
8 Ingolia et al 2011) to near complete stalling. A number of mRNAs retain 4-6 ribosomes after runoff
9 in WT, but not in FMRP-deficient slices. Some RNAs associated with FMRP-stalled ribosomes
10 encode proteins involved in neurologic function and transcriptional regulation. One such RNA
11 encodes an epigenetic regulator, SETD2, a methyltransferase for the chromatin mark H3K36me3.
12 We find an increase in SETD2 protein levels in *Fmr1*-deficient hippocampus. ChIP-seq
13 demonstrates that distribution of this mark varies in a genotype (i.e, WT vs. *Fmr1*-deficient)-
14 dependent manner in hippocampal tissue. In mammals, apart from blocking cryptic transcription
15 initiation and DNA damage response, H3K36me3 is correlated with pre-mRNA processing events
16 such as alternative splicing (Kim et al 2011; Kolasinska-Zwierz et al 2009). RNA sequencing
17 reveals that a number of splicing events such as exon skipping are altered in FMRP-deficient
18 slices, and that these transcripts are linked to neural function and autism spectrum disorders.
19 Aberrant RNA splicing of synapse related genes has in recent years been found to be widely
20 prevalent in autism spectrum disorders (Lee et al., 2016; Quesnel-Vallières et al., 2016; Smith
21 and Sadee, 2011). Our study demonstrates that a reduction in ribosome stalling in the *Fmr1*-
22 deficient brain results in a cascade of epigenetic and RNA processing changes that likely
23 contribute to neurologic disease.
24

Results

1
2
3 Hippocampal Schafer collateral-CA1 synapses exhibit an exaggerated mGluR-LTD in
4 *Fmr1*-deficient mice that is aberrantly protein synthesis-independent (Huber et al 2000). To
5 identify mRNAs whose basal level expression is misregulated, we prepared CA1-enriched
6 hippocampal slices (400 μ m thickness) (Figure 1A), performed ribosome profiling and RNA-seq
7 (Figure 1B) and calculated translational efficiency (TE), which is defined as the number of
8 ribosome footprints divided by the number of RNA-seq reads. We identified RNAs with changes
9 in TE (TE up /TE down) or RNAs whose levels were elevated or reduced but without
10 commensurate changes in TE (mRNA up/ mRNA down) (Figure 1C, Table S1) (nominal p-value<
11 0.01, false discovery rate = 0.097 by permutation test). A gene ontology (GO) functional analysis
12 of the biological processes most enriched in each regulatory group shows that the RNA down
13 group encodes factors that mediate taxis/chemotaxis, while the “mRNA up” group encodes factors
14 involved in ribonucleotide metabolism (Figure 1D, S1A,B). The “TE down” mRNAs encode factors
15 that control synaptic transmission (Figure 1D, S1C). The “mRNA down” group is enriched for
16 cellular components linked to the extracellular matrix while the “mRNA up” group encodes the
17 myelin sheath and spliceosomal-interacting factors. The “TE down” group is involved in the
18 extracellular matrix and structures involved in synaptic architecture (Figure 1E, S1C). No GO
19 terms from the TE up group were statistically significant.

20 Heat maps of the top 20 mRNAs with altered TEs both up and down in *Fmr1*-deficient
21 hippocampal slices compared to the wild type are shown in Figures 2A and B. Examples of the
22 change in TEs is depicted in Figure 2C. *Gfpt2* (glutamine-fructose-6-phosphate transaminase 2)
23 mRNA, is nearly unchanged in *Fmr1* KO but has an increase in ribosome footprints (Figure 2C).
24 Conversely *Lhfpl5* (Lipoma HMGIC fusion partner-like 5) mRNA, has reduced numbers of
25 ribosome footprints while RNA levels are mostly unchanged (Figure 2D). Neither *Gfpt2* nor *Lhfpl5*
26 mRNAs have FMRP CLIP sites. Figure 2E shows boxplots for all 843 FMRP CLIP RNAs (Darnell

1 et al 2011). As a group, these RNAs decrease significantly in *Fmr1* KO, which is tracked by
2 commensurate decreases in ribosome footprints resulting in no change in TE.

3 We compared our “TE down” and “TE up” groups in *Fmr1* KO hippocampus with results
4 from Das Sharma et al (2019), who performed ribosome profiling on mouse frontal cortex, and
5 Thomson et al (2017) who performed ribosome affinity purification (TRAP-seq) from hippocampal
6 CA1 pyramidal neurons (Figure 2F). Only 37 of our TE down RNAs were similarly detected by
7 Das Sharma et al (2017) and only 5 by Thomson et al (2017). Even fewer of our TE up RNAs
8 were detected in either of those studies (Figure 2F). We surmise that the differences in methods
9 and source material are likely responsible for little overlap among the studies.

10 Our data show almost all changes in ribosome footprint number in *Fmr1*-deficient
11 hippocampal-cortical slices can be attributed to altered RNA levels irrespective of whether the
12 transcripts are FMRP CLIP targets. This suggests that the increase in incorporation of labeled
13 amino acids into protein in *Fmr1* KO hippocampal slices (e.g., Dolen et al 2007; Udagawa et al
14 2103; Bowling et al 2019) is mostly due to changes in RNA levels and/or ribosomal transit rate
15 (see below). However, TE may not necessarily reflect protein production. For example, increased
16 initiation with no change in elongation would result in an increased density of ribosome footprints
17 and yield an elevated level of protein product (Figure 2G). If there is no change in initiation but
18 elevated elongation, the TE will appear to be reduced but the production of protein will be
19 increased. Consequently, ribosome profiling at steady state, which cannot distinguish between
20 transiting and stalled ribosomes, may inadequately represent translation if there are changes in
21 elongation. To assess whether FMRP regulates ribosome dynamics, we modified our procedure
22 to investigate temporal changes in genome-wide ribosome translocation rates.

23

24 **Ribosome run off dynamics in hippocampal-cortical slices**

25 We next performed ribosomal profiling and RNA-seq in hippocampal-cortical slices at
26 different time points after blocking initiation with homoharringtonine (HHT). HHT halts ribosomes

1 on initiation codons but allows elongating ribosomes to continue translocating until they run off
2 the mRNA (Ingolia et al 2012; Lee et al 2012). Using this assay, we aimed to determine
3 differences in ribosome translocation rates of all expressed genes in wild type tissue slices. Slices
4 were incubated with HHT for 0-60 min and ribosome transit stopped at specific times with
5 cycloheximide; the samples were then used for ribosome profiling (Figure 3A, Table S1). A
6 metagene analysis of the ribosome footprints on 1401 mRNAs with open reading frames of >3000
7 nt aligned with the start and stop codons is shown in Figure 3B. The read densities at each
8 position were normalized to the average densities of the last 500 nucleotides of the CDS and is
9 based on the P site of the ribosome footprints. Using these data, a linear regression analysis
10 between the HHT treatment time and ribosome runoff distances was used to estimate the global
11 elongation rate of 4.2 nt/sec at 30°C (Figure 3C). By comparison, the global elongation rate in
12 cultured ES cells is 1.7 nt/sec at 37°C (Ingolia et al 2011).

13 We next performed a cluster analysis of all the RNAs with respect to number of ribosome
14 protected fragments at each time point (5, 10, 30, 60 min) relative to time 0. Briefly, euclidean
15 distance was first computed, followed by hierarchical clustering using Ward's algorithm (Ward,
16 1963), and the Analysis of group similarities (ANOSIM) test (Clarke, 1993) was then used to
17 assess whether distances between clusters were statistically greater than within clusters (Figure
18 3D). The RNAs fell into two broad clusters (ANOSIM $R=0.56$, $p\text{-value}<0.001$): those whose
19 ribosome runoff occurred relatively quickly (i.e., within 5-10 min, bottom cluster), and those whose
20 runoff occurred slowly, if at all (top cluster). These two clusters were then further grouped into 3
21 sub-clusters each for 6 total sub-clusters (ANOSIM $R=0.64$, $p\text{-value}<0.001$). Sub-clusters 1-3 had
22 slow runoff times while sub-clusters 4-6 had relatively fast ribosome runoff times (Figure 3D and
23 3E). The ribosomes on RNAs in sub-cluster 2 had the slowest runoff time. We next determined
24 the ribosome runoff patterns for the RNAs in each sub-cluster (Figure 3E). For example, RNAs
25 for Alcam (activated leukocyte cell adhesion molecule), Arc (activity-regulated cytoskeleton), and
26 Nptn (neuroplastin) are present in the sub-cluster 1, Col11 (collectin subfamily 11) in sub-cluster

1 2, Nrnx3 (neurexin 3) in sub-cluster 3 and actin in sub-cluster 4 (Figure 3F). As examples, Figure
2 3G shows the ribosome footprints of Nrnx3 and actin over time; Figure S2A shows ribosome
3 footprints for additional RNAs. Although there was some CDS length dependency of the ribosome
4 runoff rates, the correlation was not linear (Figure S2B). GO term analysis showed that specific
5 biological activities were remarkably associated with each sub-cluster. Genes in sub-clusters 1
6 and 3 were closely associated with neural function such as axon development and synapse
7 organization (Figure 3H). Sub-cluster 2, which contained ribosomes with the slowest runoff rates,
8 had genes encoding the extracellular matrix, sub-cluster 4 contained genes involved in metabolic
9 functions, sub-cluster 5 was associated with RNA processing and regulation, and sub-cluster 6
10 with organelle localization, among other functions (Figure S2C). These results suggest that
11 clusters of mRNAs with specific functions have differential ribosomal transit rates.

12

13 **FMRP controls ribosome translocation on specific mRNAs**

14 To investigate whether FMRP controls ribosome stalling on specific mRNAs, we first
15 determined whether it is present in ribosome-containing complexes or “granules” as suggested
16 by earlier studies (Feng et al 1998; Khandjian et al 2004; Stefani et al 2004; El Fatimy et al 2016).
17 Extracts from cortices were treated with nonionic (NP40) or ionic (DOC) detergents, or RNase
18 and sedimented through sucrose gradients. Figure S3A shows FMRP sedimented to a “heavy”
19 ribosome-containing region of the gradient even in the presence of NP40 or RNase; DOC
20 treatment, however, stripped FMRP from ribosome-containing complexes as shown previously
21 (Stefani et al 2004; Darnell et al 2011). These data suggest that FMRP is associated with
22 ribosomes in heavy granule structures and thus could play a role in ribosome stalling.

23 We next performed sucrose gradient analysis of hippocampal slices treated with HHT for
24 30 min (Figure 4), which allows ribosomes on most genes to run off (as shown in Figure 3). Figure
25 4A shows that most FMRP co-sediments with polysomes as has been shown previously (e.g.,
26 Feng et al 1998; Stefani et al 2004), but after HHT treatment, it is more prevalent in “medium”

1 gradient fractions that correspond to 4-6 ribosomes. Other proteins (e.g., UPF1, MAP2, eEF2) do
2 not show a similar change in sedimentation (Figure S3B). A small amount of FMRP remains in a
3 “heavy” (>7 ribosomes) region of the gradient (Figure 4B). The same experiments were performed
4 with *Fmr1* KO slices (Figure 4C, D). RNA-seq of the “heavy” fractions showed that 1574 RNAs
5 and 686 RNAs were reduced or elevated, respectively, in both genotypes, indicating that heavy
6 granules contain mRNAs that are sensitive or resistant to HHT treatment (Figure 4E). *Actin* is one
7 such RNA that was sensitive to HHT that was depleted by ribosome runoff (Figure 4F), which is
8 consistent with results from the HHT time course (Figure 3F, G). *Map1b* RNA, on the other hand,
9 was enriched in the heavy polysomes by HHT treatment (Figure 4G). Figure 4H shows GO terms
10 for the RNAs depleted in the heavy fractions after runoff, which include RNA processing and other
11 factors involved in RNA metabolism. Figure 4I shows the GO terms for RNAs enriched in the
12 heavy polysomes after HHT treatment, which include factors involved in membrane and ion
13 transport.

14 In contrast to the “heavy” polysome fractions, we found genotype-specific differences in
15 the RNA-seq of the “medium” polysome fractions (Table S1). Forty-six RNAs were down-
16 regulated in HHT-treated *Fmr1* KO slices relative to WT, indicating that they are normally bound
17 by FMRP-stalled ribosomes (Figure 5A). Eight of these mRNAs encode epigenetic and
18 transcriptional regulators and 23 encode proteins specifically involved in neural function (Figure
19 5B). One example is *Ankrd12* (ankyrin repeat domain containing 12), which is depleted in the KO
20 slices following HHT treatment (Figure 5C). Figure 5C shows that after HHT treatment, *Ankrd12*
21 RNA contains fewer stalled ribosomes in the medium fractions of *Fmr1* KO slices, confirming this
22 mRNA is under FMRP regulation. Figure 5D demonstrates that compared to all RNAs, the HHT-
23 sensitive RNAs (Figure 5B) showed significant decreases in RPFs and TEs but not RNA levels in
24 *Fmr1* KO relative to WT (ribosome profiling data of these RNAs from Figure 2) showing the
25 consistency between steady state ribosome profiling and the dynamic ribosome run-off assay.

1 Finally, Figure 5E demonstrates that one of the mRNAs decreased in the “medium”
2 fraction in the *Fmr1* KO slices, *SETD2*, shows an increase in its protein levels in *Fmr1* KO
3 hippocampus relative to WT, which is expected if FMRP stalls ribosome translocation on this
4 RNA. SETD2 is the sole histone lysine methyltransferase that trimethylates the histone H3 tail on
5 the lysine36(K36) residue.

6

7 **FMRP mediated regulation of H3K36me3**

8 To investigate whether altered SETD2 levels influence gene-specific changes in
9 H3K36me3, we performed ChIP-seq from WT and *Fmr1* KO hippocampus in duplicate, combining
10 hippocampal tissue from 2 animals per biologic replicate (Figure 6A). All genotypic replicates were
11 highly correlated with each other (Figure S4A). H3K36me3 is a broad histone mark that is
12 enriched primarily in the body of the gene. To measure regions with enrichment of the mark we
13 used the SICER v1.1 package (Xu et al., 2014) that annotates ChIP signal over a stretch of DNA
14 as ‘islands’ (an island is defined as a cluster of non-overlapping consecutive DNA regions (200
15 bp windows) separated by at least a 600bp gap region of DNA with no ChIP-enriched signal
16 detected above threshold). Annotation of the H3K36me3 islands shows that they were primarily
17 present within the gene body compared to promoter proximal regions, as expected (Krogan et al
18 2003; Tiedemann et al 2016) (Figure 6B,I). Metagene analysis showed there to be no genotype-
19 specific difference in the distribution of marks overall along the gene body and no effect of gene
20 length (Figure S4B, C, D). Next, we compared the number of genes with H3K36me3 islands
21 detected between both genotypes, and found more H3K36me3 harbouring genes in the *Fmr1* KO
22 than those in the WT (Figure 6B, II; note that there may be multiple islands in a single gene). We
23 further compared the differential enrichment of the H3K36me3 islands between the genotypes
24 using SICER-df script from the SICER v1.1 package (Xu et al., 2014). We found 3008 islands with
25 decreased and 2472 islands with increased H3K36me3 in the *Fmr1* KO compared to wild type
26 hippocampus ChIP-seq (p-value < 0.0001, FDR <0.0001) (Table S2). Examples of the changes

1 of these marks that are genotype-dependent is shown in Figure 6C where H3K36me3 on *Reep4*
2 (receptor expression-enhancing protein 4) is reduced but elevated on *Tprkb* (TP53-related protein
3 kinase binding protein). The decreased islands were mostly found in intragenic regions whereas
4 the increased islands were present in higher proportion in the intergenic regions (Figure 6D)
5 demonstrating a redistribution of H3K36me3 in FXS model mice. Many of the islands, especially
6 those that decrease in *Fmr1* KO animals are found on genes linked to autism spectrum disorders
7 as defined by SFARI (Figure 6E). A subset of genes (219) showed both increased and decreased
8 islands along the length of the gene body (Figure 6E). GO term enrichment analysis of the genes
9 that have either increased or decreased H3K36me3 islands is shown in Figure 6F. Although the
10 genes that have decreased islands are quite diverse, those with increased islands are remarkably
11 enriched for genes involved in neural function such as synapse assembly and animal behavior.
12 The methylated islands also undergo genotype-specific length changes; they are significantly
13 longer in the WT compared to *Fmr1* KO (p-value <0.001, Kolmogorov-Smirnov (KS) test) (Figure
14 S4E). Our data thus show that an increase in the levels of SETD2 in the *Fmr1* KO results in
15 dysregulated H3K36me3 chromatin marks.

16

17 **FMRP regulates alternative RNA processing**

18 H3K36me3 in mammals has been correlated with alternative pre-mRNA splicing (Kim et
19 al 2011). We analyzed our RNA-seq data from WT and *Fmr1* KO hippocampal slices using rMATS
20 alternative splicing package (Shen et al., 2014) and detected many alternative pre-mRNA
21 processing events including skipped exon (SE), mutually excluded exon (MXE), alternative 5' and
22 3 splice site (A5SS and A3SS), as well as retained intron (RI) (Figure 7A, Table S3, FDR < 5%
23 and p-value<0.05). The number of exon inclusion events are shown (Differences in exon inclusion
24 levels is calculated as Percent Spliced In (PSI) and a cutoff of $|\Delta\text{PSI}| \geq 5\%$ is used). Several
25 of the exon skipping events were validated by RT-qPCR, with ~20-40% reduction in exon skipping
26 in the *Fmr1* KO relative to WT (Figure 7B). These skipped exons have previously been found to

1 be associated with defects in brain development and disease pathology (An and Grabowski, 2007;
2 Fugier et al., 2011; Rockenstein et al., 1995; Wang et al., 2018). Figure 7C shows all the RNA
3 processing events that undergo changes in *Fmr1*-deficient hippocampus relative to WT (p -
4 value <0.05 , $|\Delta\text{PSI}| \geq 5\%$). Skipped exons are by far the most prevalent category, followed by
5 alternative 3' splice sites; retained introns are the most infrequent. The genes whose RNA
6 processing events are altered in *Fmr1* KO are strongly linked to neural function such as vesicle
7 transport to synapses, vesicle recycling, etc. (Figure 7D). Moreover, many of the alternatively
8 spliced (Alt. Spl. or AS) genes in *Fmr1* KO hippocampus (Alt. Spl. *Fmr1* KO) are linked to autism
9 (i.e., SFARI autism spectrum disorder database, ASD) (Figure 7E). In addition, the AS genes in
10 *Fmr1* KO significantly overlap with genes previously found to be alternatively spliced in patients
11 with autism (Alt. Spl. ASD) (Parikshak et al., 2016) (Figure 7E). We also find an overlap of genes
12 with changes in H3K36me3 islands with those found to harbor aberrant splicing in *Fmr1* KO tissue
13 (Figure 7E). We next assessed the H3K36me3 levels at the skipped exons in the SE category
14 and found a trend towards a decrease in the H3K36me3 marks at the 5' splice site of these exons
15 that are skipped in the *Fmr1* KO hippocampus compared to the wild type (Figure 7F, p -
16 value <0.07). Thus, as with other autism spectrum disorders, dysregulated alternative splicing is
17 prevalent in a mouse model of FXS and might be linked to changes in H3K36me3.

18

19

Discussion

1
2
3
4
5
6
7
8
9
10
11
12
13
14
15
16
17
18
19
20
21
22
23
24
25
26

We used several approaches to investigate FMRP regulation of mRNA expression in the mouse brain, focusing first on steady state ribosome profiling in hippocampal slices. *Fmr1* deficiency resulted in ribosome footprint levels that mostly tracked altered levels of RNA, which is consistent with other studies (Liu et al 2018; 2019; Das Sharma et al 2019). Because ribosome profiling at steady state cannot distinguish between static and translocating ribosomes, we modified our profiling procedure (Ingolia et al 2011) to identify the dynamic range of ribosome translocation rates genome-wide in hippocampal slices. These studies in turn resulted in four main novel findings. First, they showed that mRNAs cluster into defined functional biology groups based on the transit rates of their associated ribosomes. The ribosomes on most (>5000 detectable mRNAs) transit relatively rapidly, whereas on other RNAs (~3000), ribosome transit is slow or nearly not at all (~350). There is some CDS length dependency as well. Second, using a combination of ribosome runoff and sucrose gradient centrifugation, we identified ~50 mRNAs associated with FMRP-stalled ribosomes, which strongly imply translational regulation. One of these mRNAs encodes a histone lysine methyltransferase, SETD2, which is elevated in *Fmr1* KO hippocampus. Third, the SETD2-dependent histone mark, H3K36me3, is rearranged in both intragenic and intergenic regions upon *Fmr1* deficiency. Fourth, because H3K36me3 has been correlated with alternative RNA processing in mammals (Kim et al 2011), we analyzed our RNA-seq data and found widespread aberrant splicing in the *Fmr1* KO hippocampus, most prominently exon skipping/inclusion. These altered processing events often correlated with changes in the histone mark, occurred on genes that regulate pre-synaptic functions such as synaptic vesicle recycling, and were strongly linked to autism spectrum disorders (Figure 7E).

Earlier studies have inferred that ribosome stalling in the brain is linked to RNA transport granules in dendrites (Krichevsky and Kosik 2001; Mallardo et al 2003; Kanai et al 2004; Khandjian et al 2004). It is possible that at least some of the ribosome stalling we observe may

1 be the result from such compartmentalization in neurons, or perhaps is a more general feature of
2 the brain. In contrast, rapidly dividing ES cells do not appear to have stalled ribosomes, at least
3 not of the magnitude we observe here (Ingolia et al 2011). Irrespective of whether ribosome
4 stalling is a dendritic or neuronal phenomenon, how it occurs mechanistically on specific mRNAs
5 is unclear, but it could be related to secondary structure or association with RNA binding or other
6 proteins. One clue, however, could be the accumulating evidence that strongly implicates
7 phosphorylation of eEF2 as a coordinator of translation and neural activity, and thus is likely to be
8 one mediator of ribosome translocation rates (Scheetz et al 2000; Sutton et al 2007; Park et al
9 2008; McCamphill et al 2015; Heise et al 2017). Even so, the involvement of phospho-eEF2, a
10 general translation factor, would unlikely be responsible for mRNA-specific stalling. We also noted
11 that some mRNAs, such as those in sub-cluster 2 (Figure 3D, E) encode proteins involved in the
12 extracellular matrix (Figure S2C). A number of these proteins contain proline-rich stretches,
13 whose geometry in the polypeptide exit tunnel can lead to ribosome stalling (Schuller et al 2017;
14 Hutter et al 2017).

15 We have identified ~50 mRNA whose ribosomes are stalled specifically by FMRP. These
16 RNAs include those with and without FMRP CLIP sites in coding regions, so it would appear that
17 a simple FMRP “roadblock” model would not explain ribosome stalling. Alternatively, Ishizuka et
18 al (2002) showed that *Drosophila* FMRP binds ribosomal proteins, and in a cryo-EM study, Chen
19 et al (2014) found that *Drosophila* FMRP reconstituted with mammalian ribosomes binds a region
20 that would preclude tRNA and elongation factors from engaging in translation. However attractive
21 this model is for FMRP-mediated ribosome stalling, the fact that mRNA or translation factors were
22 not included in the reconstitution assays brings into question whether it reflects the physiological
23 basis for ribosome stalling.

24 Our studies revealed that FMRP stalls ribosomes on a number of mRNAs that encode
25 epigenetic regulators and that the mis-regulation of one of them in *Fmr1*-deficient hippocampus,
26 SETD2, leads to widespread changes in H3K36me3 chromatin marks (islands). These

1 H3K36me3 islands are both enriched for and depleted from autism risk genes (Figure 6E) as well
2 as those with synaptic functions (Figure 6F). This suggests that SETD2, the only enzyme that
3 catalyzes this chromatin mark, might also be an autism risk gene, which has been previously
4 reported (Lumish et al 2015). Mutations in several chromatin remodeling genes have been linked
5 to changes in neural function, autism, and other intellectual disabilities (van Bokhoven 2011;
6 Goodman and Bonni 2019). In most cases, however, mutations in epigenetic modifiers result in
7 up or down regulation of transcription. Indeed, previously identified epigenetic changes in FXS
8 model mice by Korb et al (2017), particularly H3K4me3, H4K8ac, and H4K16ac, were responsible
9 for widespread changes in transcription in cortical neurons and the cerebellum. Importantly, these
10 investigators could rescue several FXS pathophysiologies, many of which resemble those in
11 autism, by targeting the epigenetic reader protein Brd4. H3K36me3 does not mark promoter
12 regions, but instead is found in gene bodies and increases as RNA polymerase II proceeds 3'
13 during catalysis (Neri et al 2017). In mammals, one of the functions H3K36me3 is correlated with,
14 if not causative for, alternative pre-mRNA processing (Kim et al 2011). In the *Fmr1*-deficient
15 hippocampus, we detected extensive changes in RNA processing, mostly exon skipping.
16 Surprisingly, most of the skipped exons occurred in genes that have pre-synaptic functions such
17 as synaptic vesicle recycling, transport, exocytosis, etc., which could at least partially explain
18 alterations in synaptic vesicle dynamics and neurotransmitter release in FXS model mice (Deng
19 et al 2013; Ferron et al 2014; Broek et al 2016). Furthermore, a number of skipped exons in *Fmr1*
20 KO have been linked to neurological disorders such as Alzheimer's disease (skipped exon 7 in
21 *APP* (Fragkouli et al., 2017; Rockenstein et al., 1995)), Parkinson's disease (skipped exon 3 in
22 *Mapt* (Lai et al., 2017)), and intellectual disabilities (skipped exon12 in *Cnksr2* (Houge et al.,
23 2012)).

24 Alternative pre-mRNA processing is a common feature in autism (Quesnel-Vallieres et al
25 2019), so it is perhaps not surprising that this would occur in Fragile X. However, because FMRP
26 is an RNA binding protein that regulates translation, a reasonable assumption would be that

1 mRNAs encoding splicing factors are improperly expressed in the disorder, and that this leads
2 directly to misplicing events. However, our data indicate that this relationship might not be linear.
3 Instead, we find that FMRP controls ribosome dynamics on specific mRNAs, which leads to
4 elevated translation (e.g., SETD2), which leads to chromatin modifications (e.g., H3K36me3),
5 which in turn might lead to alternative splicing of neuronal mRNAs (Figure 7G). These
6 observations do not preclude the possible, if not likely, direct involvement of FMRP in some of
7 these events. Even so, inferences that Fragile X is a disorder of improper translation, while not
8 incorrect, is vastly oversimplified. However, the complexity of gene expression changes in Fragile
9 X might offer opportunities for therapeutic intervention at multiple steps.

10

1 MATERIAL AND METHODS

2 Mouse acute brain slice preparation

3 Mouse protocols were reviewed and approved by the institutional animal care and use committee
4 (IACUC) and all colonies were maintained following animal research guidelines. Transverse
5 hippocampal or hippocampal-cortical brain slices were acutely prepared from P28-35 C57BL/6N
6 wild-type or *Fmr1* KO male mice littermates as previously described (Guo et al., 2016). Briefly,
7 mice were anesthetized with ketamine (125 mg/kg)/xylazine (25 mg/kg) and transcardially
8 perfused with chilled (4°C) sucrose dissection buffer containing the following (in mM): 2.6 KCl,
9 1.25 NaH₂PO₄, 26 NaHCO₃, 0.5 CaCl₂, 5 MgCl₂, 212 mM sucrose, and 10 dextrose aerated with
10 95% O₂/5% CO₂. Transverse hippocampal slices (400µm) were obtained on a Leica VT1200S
11 slicer. For ribosomal profiling experiments (Figure 1), CA3 was cut off to enrich for CA1 and for
12 each biological replicate, 8-10 slices from 6-8 mice/genotype were pooled. Slices were recovered
13 and maintained at 30°C for 3-4 hours in artificial cerebrospinal fluid (ACSF) which contained the
14 following (in mM): 119 NaCl, 2.5 KCl, 2 CaCl₂, 1 MgCl₂, 26 NaHCO₃, 1 NaH₂PO₄ and 11 D-glucose
15 aerated with 95%/O₂/5% CO₂ to pH 7.4. Slices were then treated with cycloheximide (100 µg/ml)
16 in ACSF, 4°C, snap-frozen on dry ice/EtOH bath, and stored at -80°C. For homoharringtonine
17 (HHT) experiments (Figures 3-5), cortical-hippocampal slices were recovered 3-4 hours in ACSF
18 and then treated with HHT (20 µM) (Tocris) or 0.05% DMSO (vehicle) for different times (0, 5, 10,
19 30, 60 min). At the end of the incubation time, slices were snap/frozen on dry ice/EtOH bath and
20 stored at -80 C. Ten slices from 2-3 mice/genotype were pooled for each biological replicate.

21

22 Sucrose gradients of hippocampal slices for steady-state ribosome profiling

23 Frozen, isolated CA1 hippocampal slices were thawed in ice-cold homogenization buffer (20mM
24 Tris-HCl pH7.4, 5mM MgCl₂, 100mM KCl, 1mM DTT, 100µg/ml CHX (cycloheximide), 25U/ml
25 Turbo DNaseI (Ambion, #AM2238), 1X EDTA-free protease inhibitor (Roche), avoiding detergent
26 in nuclease-free water) on ice for 5min. Wide orifice tips were used to transfer slices to a pre-

1 chilled detergent-free Dounce homogenizer. Tissues were slowly homogenized by hand (20
2 strokes of loose pestle A, and 20 strokes of tight pestle B). Homogenates were carefully
3 transferred to clean 1.5ml tubes with clean glass Pasteur pipets and bulbs. 1% NP-40 was added
4 to the homogenates and incubated on ice for 10min. Homogenates were clarified by centrifugation
5 at 2,000g 4 °C for 10min. The supernatants were collected and clarified again by centrifugation
6 at 20,000g 4 °C for 10min. The supernatants were collected, and the amounts of nucleic acid
7 were measured by Nanodrop (A_{260} units). For each sample, cytoplasmic RNA for RNA-seq was
8 purified from one-fourth of the lysate with TRIzol LS reagent (Invitrogen, #10296028). The other
9 three-fourths of the lysate was digested with 100ng RNase A (Sigma, # R4875) and 60U RNase
10 T1 (Thermo Fisher Scientific, #EN0542) per A_{260} at 25°C for 30 min and stopped by chilling on
11 ice and adding 50U SUPERase In RNase inhibitor (Ambion, #AM2694). Digested lysates were
12 applied to 10%-50% (w/v) sucrose gradients prepared in 1X polysome buffer (20mM Tris-HCl
13 pH7.4, 5mM $MgCl_2$, 100mM KCl, 1mM DTT, 100 μ g/ml CHX in nuclease-free water). After the
14 ultracentrifugation in a SW41Ti rotor (Beckman Coulter) at 35,000 rpm (avg 151,263g) 4°C for
15 2.5 hours, gradients were fractionated at 1.5 ml/min and 12 sec collection intervals through a
16 fractionation system (Brandel) that continually monitored A_{260} values. Monosome fractions were
17 identified, pooled, and extracted with TRIzol LS.

18

19 **Sucrose gradients of cortical-hippocampal slices for run-off ribosome profiling**

20 Frozen cortical-hippocampal slices were thawed in ice-cold lysis buffer (20mM Tris-HCl pH7.4,
21 5mM $MgCl_2$, 100mM KCl, 1mM DTT, 100 μ g/ml CHX, 25U/ml Turbo DNaseI, 1X EDTA-free
22 protease inhibitor, 1% NP-40, in nuclease-free water) on ice for 5min. Tissues were dissociated
23 by pipetting and further trituration through 25G needle for 10 times. Lysates were incubated on
24 ice for 10min and then clarified by centrifugation at 2,000g 4 °C for 10min. The supernatants were
25 collected and clarified again by centrifugation at 20,000g 4 °C for 10min. The supernatants were
26 collected, and the amounts of nucleic acid were measured with Qubit HS RNA assays. Lysates

1 containing ~40µg RNA were digested with 600ng RNase A (Ambion, #AM2270) + 75U RNase T1
2 (Thermo Fisher Scientific, #EN0542) /µg RNA in 0.3ml at 25°C for 30min and stopped by chilling
3 on ice and adding 50U SUPERase In RNase inhibitor. Digested lysates were applied to 10%-50%
4 (w/v) sucrose gradients similarly as above.

5

6 **Sucrose gradients of cortical-hippocampal slices for polysome profiling**

7 Frozen cortical-hippocampal slices were thawed in ice-cold homogenization buffer on ice for 5min.
8 Wide orifice tips were used to transfer slices to a pre-chilled detergent-free Dounce homogenizer.
9 Tissues were gently homogenized by hand (3 strokes of loose pestle A, and 7 strokes of tight
10 pestle B). Homogenates were carefully transferred to clean 1.5ml tubes with clean glass Pasteur
11 pipets and bulbs. Homogenates were clarified by centrifugation at 2,000g 4 °C for 10min. The
12 supernatants were collected and clarified again by centrifugation at 10,000g 4 °C for 10min. The
13 supernatants were collected, and the amounts of nucleic acid were measured with Nanodrop (A_{260}
14 units). 1% NP-40 was added to the homogenates and incubated on ice for 10min. ~1 A_{260} unit of
15 lysate was saved for the input RNA. ~5 A_{260} units of lysate were applied to 15%-45% (w/w)
16 sucrose gradients prepared in 1X polysome buffer and with the lower block mark and long cap.
17 After the ultracentrifugation in a SW41Ti rotor (Beckman Coulter) at 35,000 rpm (avg 151,263g)
18 4°C for 2 hours, gradients were fractionated at 1.5 ml/min and 20 sec collection intervals through
19 a fractionation system (Brandel) that continually monitored A_{260} values. Some gradients were
20 treated with RNase A prior to centrifugation.

21

22 **Ribosome profiling**

23 Ribosome profiling libraries were prepared following the published protocols (Heyer et al., 2015).
24 Briefly, rRNA was depleted from the purified monosomal RNA with RiboZero (Illumina,
25 #MRZG12324). Remaining RNA samples were separated on a 15% TBU gel (National
26 Diagnostics, #EC-833) and the ribosome footprints were size-selected between the 26 and 34nt

1 markers. RNA was eluted from the crushed gel pieces in RNA elution buffer (300mM NaOAc
2 pH5.5, 1mM EDTA, 0.25% SDS) at room temperature overnight, filtered with Spin-X Centrifuge
3 Tube Filters (Corning, #8162) and precipitated with equal volume of isopropanol. Recovered RNA
4 was dephosphorylated with T4 Polynucleotide Kinase (NEB, #M0201S) and ligated with
5 preadenylated adaptor in miRCat®-33 Conversion Oligos Pack (IDT) using T4RNL2Tr.K227Q
6 ligase (NEB, #M0351L). Reverse transcription (RT) was performed with primers containing 5nt-
7 barcodes and 8nt-unique molecular identifiers (UMIs) and SuperScript III (Invitrogen, #18080-
8 044) in 1X first-strand buffer without MgCl₂ (50 mM Tris-HCl, pH 8.3, 75 mM KCl). RT products
9 were separated on a 10% TBU gel and the 130-140nt region was selected. cDNA was eluted in
10 DNA elution buffer (10mM Tris pH 8.0, 300mM NaCl, 1mM EDTA) at room temperature overnight,
11 filtered, and precipitated with isopropanol. Purified cDNA was circularized with CirLigase
12 (Epicentre, #CL4115K). Except for the RNase titration samples, cDNA derived from remaining
13 rRNA was hybridized to biotin-labelled antisense probes (IDT) and further depleted with
14 Dynabeads MyOne Streptavidin C1 (Invitrogen, #65001). Optimal PCR cycle number was
15 determined empirically by test PCR reactions with titrated cycle numbers. Final PCR amplification
16 was performed with KAPA Library Amplification Kit (Kapa Biosystems, #KK2611) and 180-190bp
17 products were size-selected on an 8% TBE gel. DNA was eluted in DNA elution buffer, filtered,
18 and precipitated with isopropanol. The final library DNA was purified with AMPure XP beads
19 (Beckman Coulter, #A63880). Oligos used for the library preparation are listed in Table S2.

20 In parallel, input RNA samples were processed similarly as the ribosome footprints except
21 the following steps. After rRNA depletion, input RNA mixed with an equal volume of 2x alkaline
22 fragmentation solution (2 mM EDTA, 10 mM Na₂CO₃, 90 mM NaHCO₃, pH ~ 9.3) and heated at
23 95°C for 15min to achieve an average fragment length of ~140nt. Fragmented RNA samples were
24 separated on a 10% TBU gel and size-selected between the 100 and 150nt markers. RT products
25 were separated on a 10% TBU gel and the 200-250nt region was selected. Antisense probe

1 depletion was omitted for input RNA samples. 260-300bp final PCR products were size-selected
2 on an 8% TBE gel.

3 The size distributions of final libraries were measured by Fragment Analyzer (Advanced
4 Analytical, performed by Molecular Biology Core Labs at UMMS). The concentrations were
5 quantified with KAPA Library Quantification Kit (Kapa Biosystems, #KK4835). Libraries were
6 pooled with equal molar ratios, denatured, diluted, and sequenced with NextSeq 500/550 High
7 Output Kit v2 (Illumina, 75bp single-end runs, #FC-404-2005) on a Nextseq500 sequencer
8 (Illumina).

9

10 **RNA-seq for polysome fractions**

11 Based on the FMRP signals in the immunoblotting of gradient fractions, medium and heavy
12 fractions were identified, pooled, and extracted with TRIzol LS together with saved input lysates.
13 RNA samples were quantified with Qubit HS RNA assay kit and the integrity was examined with
14 Fragment Analyzer. 200ng RNA was used for BIOC Rapid directional qRNA-seq library
15 preparation following the manufacturer's instructions. 12 cycles were used for the final PCR
16 amplification. The libraries were quantified with KAPA Library Quantification Kit and the quality
17 was examined with Fragment Analyzer. Libraries were pooled with equal molar ratios, denatured,
18 diluted, and sequenced with NextSeq 500/550 High Output Kit v2 (Illumina, 80bp pair-end runs
19 for RNA-seq, #FC-404-2002) on a Nextseq500 sequencer (Illumina).

20

21 **Ribosome profiling read mapping**

22 Individual samples were separated from the raw fastq files based on the barcode sequences.
23 Adaptor sequences
24 (TGGAATTCTCGGGTGCCAAGGAGATCGGAAGAGCGGTTCAGCAGGAATGCCGAGACCG)
25 were removed with cutadapt (1.7.1). Trimmed fastq files were uploaded to the Dolphin platform
26 (<https://www.umassmed.edu/biocore/introducing-dolphin/>) at the UMMS Bioinformatics Core for

1 the mapping steps. Trimmed reads were quality filtered with Trimmomatic (0.32) and mapped to
2 the mouse rRNA and then tRNA references with Bowtie2 (2.1.0). Unmapped reads were next
3 mapped to the mm10 mouse genome with Tophat2 (2.0.9). Reads mapped to >1 loci of the
4 genome were classified as “multimapped” reads and discarded. PCR duplicates were marked
5 based on the UMI sequences with custom scripts and only uniquely mapped reads without
6 duplicates were retained with Samtools (0.0.19) for the downstream analyses. RPF length
7 distribution, P-site offsets, and frame preference were calculated with plastid (0.4.8). Counts at
8 each nucleotide position were extracted using P-sites of RPFs and 5'end of mRNA reads with
9 +11 offset, normalized to the library size, averaged across replicates, and plotted along mRNA
10 positions with custom scripts.

11

12 **Steady-state differential translation analysis**

13 Cleaned bam files were converted to fastq files with bedtools. For both ribosome profiling and
14 RNA-seq, gene expression was quantified with RSEM (1.2.11) using the cleaned fastq files and
15 Refseq (V69) mouse CDS without the first and last 30nt to avoid the translation initiation and
16 termination peaks. Genes were filtered with minimum 10 reads across all replicates and then the
17 read counts were batch-corrected with the Combat function in sva (3.24.4) using a full model
18 matrix. Batch-corrected counts were normalized with trimmed mean of M values (TMM) method
19 and used to identify differential expressed genes (DEGs) with anota2seq (1.0.0). Instead of the
20 default setting, the priority of TE groups were set to be higher than that of mRNA only groups. A
21 permutation test was performed to estimate the false discovery rate (FDR) with nominal p-value
22 < 0.01, which was 0.097. GO analysis was performed and plotted with clusterProfiler (3.10.1)
23 using all genes past filtering in the dataset as the background.

24

25 **Hierarchical clustering of ribosome run-off and gene ontology (GO) enrichment of each** 26 **cluster**

1 To categorize and group genes with distinct ribosome run-off patterns, the RPF of each gene at
2 each time point was first normalized to time point 0. The Euclidean distance matrix was then
3 calculated, followed by hierarchical clustering using Ward's agglomeration method (Ward, 1963).
4 The clustering process was performed using the hclust (Galili, 2015), and the clustering heatmap
5 was displayed using pheatmap (Kolde and Kolde, 2015) in R. To test the reliability of clustering,
6 analysis of group similarities (ANOSIM) test (Clarke, 1993) was performed using vegan (Dixon,
7 2003) in R with 1000 permutation times on both overall clusters and sub-clusters. The global
8 pattern of each cluster was summarized using the corresponding median and standard deviation
9 in each timepoint.

10 GO enrichment analysis for each sub-cluster were performed through clusterProfiler (Yu
11 et al., 2012) using genes covered by run-off ribosome profiling as background. The statistical
12 significance was adjusted using FDR. To remove redundancy in reporting, each reported GO term
13 was required to have at least 25% of genes that were not associated to another term with a more
14 significant p value.

15 **Western blotting**

16 Hippocampi were homogenized at 4°C in RIPA buffer. Protein complexes were released by
17 sonication at 4°C and the extract was centrifuged at 13,200 rpm for 10 min at 4°C and the
18 supernatant collected. Protein concentration was determined by BCA reagent. Proteins (10 µg)
19 were diluted in SDS-bromophenol blue reducing buffer with 40 mM DTT and analyzed using
20 western blotting with the following antibodies: SETD2 (ABclonal, A11271) and Lamin AC (Thermo
21 Fisher, 14-9688-80). After incubation in primary antibody, immunoblots were incubated with HRP-
22 conjugated secondary antibodies (Jackson ImmunoResearch) and developed by Clarity ECL
23 substrate (Biorad). For sucrose gradient fractions, 60µl samples were mixed with 20µl 4X SDS
24 loading dye (240mM Tris-HCl pH 6.8, 5% beta-mercaptoethanol, 8% SDS, 40% glycerol, 0.04%
25 bromophenol blue) and boiled at 95°C for 10min. Samples were briefly heated at 95°C again for

1 30sec immediately before loading on 10% SDS-PAGE gel (35 μ l/sample). Separated proteins
2 were transferred to PVDF membranes at constant 90 mA 4°C for 16 hours. Membranes were
3 blocked with 5% non-fat milk in 1X TBST at room temperature for 1hour and incubated with
4 primary antibody at 4°C overnight. FMRP (Abcam, 1: 2000), Tubulin (Sigma, 1:5000), Rpl4
5 (Proteintech, 1:5000), UPF1 (Abcam, 1: 5000), MAP2 (Millipore, 1:2000), eEF2 (Cell signaling,
6 1:2000), GAPDH (Cell signaling, 1:2000), MRPS18B (Proteintech, 1:2000) and Rps6 (Cell
7 signaling, 1:4000) were diluted in 1X TBST with 5% non-fat milk. Membranes were washed three
8 times for 10min with 1XTBST and incubated with anti-rabbit or anti-mouse secondary antibodies
9 (Jackson, 1:10000) at room temperature for 1hour. Membranes were washed three times for
10 10min with 1XTBST, developed with ECL-Plus (Pierce), and scanned with GE Amersham Imager

11 **Chromatin immunoprecipitation Sequencing (ChIP-Seq)**

12 ChIP was performed as previously described (Cotney and Noonan, 2015). Briefly,
13 hippocampal tissue was isolated from 4 adult mice (P35) per genotype and minced into tissue <
14 0.5mm³ in 250ul of ice-cold PBS with protease inhibitors. Tissue was cross-linked with 1%
15 formaldehyde and rotated at room temperature for 15 min at 50 rpm and quenched with 150mm
16 glycine for 10 min in a total volume of 1ml PBS. The supernatant was discarded after
17 centrifugation at 2000g for 10 min at 4°C and the pellet was resuspended in 300ul of chilled cell
18 lysis buffer for 20 min on ice. Swollen pellets were homogenized using a glass Dounce
19 homogenizer (2ml) with 40 strokes of a tight pestle on ice. Nuclei were harvested after
20 centrifugation at 2000g for 5min at 4°C and resuspended in 300ul ice-cold nuclear lysis buffer for
21 20min on ice. SDS was added to make a final concentration of 0.5%. Samples were sonicated on
22 a Bioruptor® sonicator at high power settings for 9 cycles (sonication: 30 sec on, 90 sec off) of
23 15min each at 4°C at high power. Supernatants were collected after centrifugation at 16,000g for
24 10 min at 4°C. The samples were diluted to bring the SDS concentration <0.1%; 10% of each
25 sample was reserved as input. The rest of the samples were divided into two and incubated with

1 Protein G dynabeads coupled overnight at 4⁰C with either H3K36me3 (Abcam ab9050, 5µg per
2 CHIP) or IgG (Sigma 12-371, 5 µg per CHIP). After IP, beads were washed, and chromatin eluted
3 in elution buffer for 20 min shaking at 65°C. IP and Input samples were de-crosslinked overnight
4 at 65°C. RNase digestion for 1 hr. at 37°C and proteinase K treatment for 30 min at 55°C was
5 performed. DNA was then purified with the QIAGEN PCR purification kit in 50ul elution buffer. For
6 library preparation, purified input and IP DNA was end repaired using T4 DNA polymerase,
7 Klenow polymerase and T4 Polynucleotide kinase from NEB at 20°C for 30 min. DNA was
8 extracted using 35ul of the Agencourt Ampure XP beads and 'A' bases were added to the 3' end
9 using Klenow exonuclease (3' to 5' exo minus) from NEB for 30min at 37°C. DNA was purified
10 using 60ul of the Agencourt Ampure XP beads and Illumina adapter sequences were ligated to
11 the DNA fragments using the Quick Ligase (NEB) for 15min at 20°C. The library was size-selected
12 using 50ul of Agencourt Ampure XP beads. Using the multiplexing barcoded primers, the library
13 was PCR amplified and purified using 50ul of the Agencourt Ampure XP beads and analyzed
14 using a Fragment Analyzer (Advanced Analytical, performed by Molecular Biology Core Labs at
15 UMMS). Libraries were pooled with equal molar ratios, denatured, diluted, and sequenced with
16 NextSeq 500/550 High Output Kit v2.5 (Illumina, 75bp paired-end runs,) on a Nextseq500
17 sequencer (Illumina).

18

19 **ChIP-Seq analysis**

20 For ChIP-sequencing analysis, alignments were performed with Bowtie2 (2.1.0) using the mm10
21 genome, duplicates were removed with Picard and TDF files for IGV viewing were generated
22 using a ChIP-seq pipeline from DolphinNext (Yukselen et al., 2019). The broad peaks for
23 H3K36me3 ChIP-Seq were called using the SICER v1.1 package (Xu et al., 2014). H3K36me3
24 enriched islands were identified using the parameters set to a window size of 200bp, gap size
25 600bp and FDR cutoff of 1×10^{-3} , and the default value for the redundant rate cutoff. Significantly

1 enriched islands for each genotype were identified using the sicer-df.sh script with an FDR cutoff
2 of 1×10^{-3} . Gene Ontology (GO) enrichment analysis was performed using the clusterProfiler
3 package (Yu et al., 2012) to obtain GO terms related to Biological processes in the genes with
4 differentially enriched islands in the *Fmr1* KO vs Wild type. deepTools was used to plot heatmaps
5 and profiles for genic distribution of H3K36me3 ChIP signal. Samtools (0.1.19) was used for
6 sorting and converting Bam files. RPGC (per bin) = number of reads per bin / scaling factor for 1x
7 average coverage was used for normalization where the scaling factor was determined using
8 sequencing depth: (total number of mapped reads x fragment length) / effective genome size.
9 IGV tools (2.3.67) was used for visualizing TDF files and all tracks shown are normalized for total
10 read coverage. To quantify the H3K36me3 level for each gene, we calculated ChIP reads density
11 in TSS regions divided by the corresponding value in the gene body. To quantify the H3K36me3
12 level at the 5' and 3' splicing sites of the SE, the read density of ± 50 bp at each splice site was
13 normalized to the read density in the entire gene body, which controls for any fluctuations in total
14 H3K36me3 at the respective genes between both genotypes.

15

16 **Alternative splicing analysis**

17 RNA-seq from hippocampal slices was used to analyze alternative splicing (AS) using the rMATS
18 package v3.2.5 (Shen et al., 2014) with default parameters and reads were trimmed to 50bp. The
19 Percent Spliced In (PSI) levels or the exon inclusion levels calculated by rMATS using a
20 hierarchical framework. To calculate the difference in PSI between genotypes a likelihood-ratio
21 test was used. AS events with an FDR < 5% and $|\text{deltaPSI}| \geq 5\%$ as identified using rMATS were
22 used for further analysis. We included genes that had at least one read at the differential splice
23 junction for both genotypes. GO enrichment analysis was done by the clusterProfiler package (Yu
24 et al., 2012) to obtain GO term enrichment for the AS events. The genes with significant skipped
25 exons were used for validation using RT-qPCR analysis. One ug of RNA from hippocampal tissue
26 was used to generate cDNA using the Quantitech two-step cDNA synthesis kit. Primers were

1 designed to overlap skipped/inclusion exon junctions and qPCR was performed using the Bio-
2 Rad SYBR reagent on a Quantstudio3 instrument.

3 **Quantification and statistical analysis**

4 All grouped data are presented as mean \pm s.e.m. Student's t test was used to determine statistical
5 significance between groups. The Kolmogorov-Smirnov (K-S) test was used to compare the
6 distributions in the volcano plots. When exact p values are not indicated, they are represented as
7 follows: *, $p < 0.05$; **, $p < 0.01$; ***, $p < 0.001$; n.s., $p > 0.05$.

9 **Data and software availability**

10 Codes and scripts used for quantification analysis were written in Python or R and will be provided
11 upon request to the Lead Contact. Data Resources Sequencing datasets generated in this study
12 have been deposited into the GEO database under the accession number GEO:

14 **Acknowledgements**

15 We thank Lori Lorenz, Craig Peterson, Huan Shu and Danesh Moazed for valuable discussions.
16 JDR, KMH, BL, and SS conceived various aspects of the project. BL, GM, SS performed the
17 experiments. RW provided essential help with bioinformatics. JDR wrote the manuscript with input
18 from all authors. This work was supported by grants from the NIH (U54HD82013 to JDR,
19 U54HD082008 to KMH), the Simons Foundation for Autism Research Initiative (to JDR and KMH),
20 and the Charles H. Hood Foundation (to JDR). SS was supported by a postdoctoral fellowship
21 from the FRAXA Foundation.

22

23

24

REFERENCES

- An, P., and Grabowski, P.J. (2007). Exon silencing by UAGG motifs in response to neuronal excitation. *PLoS Biol.* 5, e36.
- Anderson, B.R., Chopra, P., Suhl, J.A., Warren, S.T., and Bassell, G.J. (2016). Identification of consensus binding sites clarifies FMRP binding determinants. *Nucleic Acids Res.* 44, 6649-6659.
- Ascano, M. Jr., Mukherjee, N., Bandaru, P., Miller, J.B., Nusbaum, J.D., Corcoran, D.L., Langlois, C., Munschauer, M., Dewell, S., Hafner, M., Williams, Z., Ohler, U., and Tuschl, T. (2012). FMRP targets distinct mRNA sequence elements to regulate protein expression. *Nature* 492, 382-386.
- Bowling, H., Bhattacharya, A., Zhang, G., Alam, D., Lebowitz, J.Z., Bohm-Levine, N., Lin, D., Singha, P., Mamcarz, M., Puckett, R., Zhou, L., Aryal, S., Sharp, K., Kirshenbaum, K., Berry-Kravis, E., Neubert, T.A., and Klann, E. (2019). Altered steady state and activity-dependent de novo protein expression in fragile X syndrome. *Nat. Commun.* 10, 1710.
- Brar, G.A., and Weissman, J.S. (2015). Ribosome profiling reveals the what, when, where and how of protein synthesis. *Nat. Rev. Mol. Cell Biol.* 16, 651-664.
- Broek JAC, Lin Z, de Gruiter HM, van 't Spijker H, Haasdijk ED, Cox D, Ozcan S, van Cappellen GWA, Houtsmuller AB, Willemsen R, de Zeeuw CI, Bahn S. (2016). Synaptic vesicle dynamic changes in a model of fragile X. *Mol Autism.* 7, 17.
- Chen, E., Sharma, M.R., Shi, X., Agrawal, R.K., and Joseph, S. (2014). Fragile X mental retardation protein regulates translation by binding directly to the ribosome. *Mol. Cell* 54, 407-417.
- Clarke, K.R. (1993). Non-parametric multivariate analyses of changes in community structure. *Australian J. Ecol.* 18, 117-143.

Cotney, J.L., and Noonan, J.P. (2015). Chromatin immunoprecipitation with fixed animal tissues and preparation for high-throughput sequencing. *Cold Spring Harb. Protoc.* 2015, 191–199.

Darnell, J.C., Van Driesche, S.J., Zhang, C., Hung, K.Y., Mele, A., Fraser, C.E., Stone, E.F., Chen, C., Fak, J.J., Chi, S.W., Licatalosi, D.D., Richter, J.D., and Darnell, R.B. (2011). FMRP stalls ribosomal translocation on mRNAs linked to synaptic function and autism. *Cell* 146, 247-261.

Das Sharma, S., Metz, J.B., Li, H., Hobson, B.D., Hornstein, N., Sulzer, D., Tang, G., and Sims, P.A. (2019). Widespread alterations in translation elongation in the brain of juvenile Fmr1 knockout mice. *Cell Rep.* 26, 3313-3322.

Deng, P.Y., Rotman, Z., Blundon, J.A., Cho, Y., Cui, J., Cavalli, V., Zakharenko, S.S., and Klyachko, V.A. (2013). FMRP regulates neurotransmitter release and synaptic information transmission by modulating action potential duration via BK channels. *Neuron* 77, 696-711.

Dixon, P. (2003). VEGAN, a package of R functions for community ecology. *J. Vegetation Science* 14, 927-930.

Dölen G, Osterweil E, Rao BS, Smith GB, Auerbach BD, Chattarji S, Bear MF. (2007). Correction of fragile X syndrome in mice. *Neuron* 56, 955-962.

El Fatimy R, Davidovic L, Tremblay S, Jaglin X, Dury A, Robert C, De Koninck P, Khandjian EW. (2016). Tracking the fragile X mental retardation protein in a highly ordered neuronal ribonucleoparticles population: a link between stalled polyribosomes and RNA granules. *PLoS Genet.* 12, e1006192.

Feng, Y., Absher, D., Eberhart, D.E., Brown, V., Malter, H.E., and Warren, S.T. (1997). FMRP associates with polyribosomes as an mRNP, and the I304N mutation of severe fragile X syndrome abolishes this association. *Mol. Cell* 1, 109-118.

Ferron, L., Nieto-Rostro, M., Cassidy, J.S., and Dolphin, A.C. (2014). Fragile X mental retardation protein controls synaptic vesicle exocytosis by modulating N-type calcium channel density. *Nat Commun.* 5, 3628.

Fragkouli, A., Koukouraki, P., Vlachos, I.S., Paraskevopoulou, M.D., Hatzigeorgiou, A.G., and Doxakis, E. (2017). Neuronal ELAVL proteins utilize AUF-1 as a co-partner to induce neuron-specific alternative splicing of APP. *Sci. Rep.* 7, 44507.

Fugier, C., Klein, A.F., Hammer, C., Vassilopoulos, S., Ivarsson, Y., Toussaint, A., Tosch, V., Vignaud, A., Ferry, A., Messaddeq, N., et al. (2011). Misregulated alternative splicing of BIN1 is associated with T tubule alterations and muscle weakness in myotonic dystrophy. *Nat. Med.* 17, 720–725.

Galili, T. (2015). dendextend: an R package for visualizing, adjusting and comparing trees of hierarchical clustering. *Bioinformatics* 31, 3718-3720.

Graber TE, Hébert-Seropian S, Khoutorsky A, David A, Yewdell JW, Lacaille JC, Sossin WS. (2013). Reactivation of stalled polyribosomes in synaptic plasticity. *Proc Natl Acad Sci U S A.* 110, 16205-16210.

Greenblatt, E.J., and Spradling, A.C. (2018). Fragile X mental retardation 1 gene enhances the translation of large autism-related proteins. *Science* 361, 709-712.

Guo, W., Molinaro, G., Collins, K.A., Hays, S.A., Paylor, R., Worley, P.F., Szumlinski, K.K., and Huber, K.M. (2016). Selective disruption of metabotropic glutamate receptor 5-homer interactions mimics phenotypes of fragile X syndrome in mice. *J Neurosci* 36, 2131-2147.

Guo, W., Zhang, L., Christopher, D.M., Teng, Z.Q., Fausett, S.R., Liu, C., George, O.L., Klingensmith, J., Jin, P., and Zhao, X. (2011). RNA-binding protein FXR2 regulates adult hippocampal neurogenesis by reducing Noggin expression. *Neuron* 70, 924-938.

Heise, C., et al. (2017). eEF2K/eEF2 pathway controls the excitation/inhibition balance and susceptibility to epileptic seizures. *Cereb Cortex* 27, 2226-2248.

Heyer, E.E., Ozadam, H., Ricci, E.P., Cenik, C., and Moore, M.J. (2015). An optimized kit-free method for making strand-specific deep sequencing libraries from RNA fragments. *Nucleic Acids Res* 43, e2.

Houge, G., Rasmussen, I.H., and Hovland, R. (2012). Loss-of-function CNKSR2 mutation is a likely cause of non-syndromic X-linked intellectual disability. *Mol. Syndromol.* 2, 60-63.

Huber, K.M., Kayser, M.S., and Bear, M.F. (2000). Role for rapid dendritic protein synthesis in hippocampal mGluR-dependent long-term depression. *Science* 288, 1254-1257.

Hutter, P., et al. (2017). Structural basis for polyproline-mediated ribosome stalling and rescue by the translation elongation factor EF-P. *Mol. Cell* 68, 515-527.

Ingolia, N.T. (2014). Ribosome profiling: new views of translation, from single codons to genome scale. *Nat. Rev. Genet.* 15, 205-213.

Ingolia, N.T., Ghaemmaghami, S., Newman, J.R., and Weissman, J.S. (2009). Genome-wide analysis in vivo of translation with nucleotide resolution using ribosome profiling. *Science* *324*, 218-223.

Ingolia, N.T., Lareau, L.F., and Weissman, J.S. (2011). Ribosome profiling of mouse embryonic stem cells reveals the complexity and dynamics of mammalian proteomes. *Cell* *147*, 789-802.

Ishizuka, A., Siomi, M.C. and Siomi, H. (2002). A *Drosophila* fragile X protein interacts with components of RNAi and ribosomal proteins. *Genes Dev.* *16*, 2497-2508.

Kanai Y, Dohmae N, Hirokawa N. (2004). Kinesin transports RNA: isolation and characterization of an RNA-transporting granule. *Neuron* *43*, 513-525.

Khandjian EW, Huot ME, Tremblay S, Davidovic L, Mazroui R, Bardoni B. (2004). Biochemical evidence for the association of fragile X mental retardation protein with brain polyribosomal ribonucleoparticles. *Proc Natl Acad Sci U S A.* *101*, 13357-13362.

Khandjian, E.W., Corbin, F., Woerly, S., and Rousseau, F. (1996). The fragile X mental retardation protein is associated with ribosomes. *Nat. Genet.* *12*, 91-93.

Kim, S., Kim, H., Fong, N., Erickson, B., and Bentley, D.L. (2011). Pre-mRNA splicing is a determinant of histone H3K36 methylation. *Proc Natl Acad Sci U S A.* *108*, 13564-13569.

Kolasinska-Zwierz, P., Down, T., Latorre, I., Liu, T., Liu, X.S., and Ahringer, J. (2009). Differential chromatin marking of introns and expressed exons by H3K36me3. *Nat Genet.* *41*, 376-381.

Kolde, R., and Kolde, M.R. (2015). Package 'pheatmap'. R Package *1*.

Korb, E., Herre, M., Zucker-Scharff, I., Gresack, J., Allis, C.D., and Darnell, R.B. (2017). Excess translation of epigenetic regulators contributes to fragile X syndrome and is alleviated by Brd4 inhibition. *Cell* 170, 1209-1223.

Krichevsky AM, Kosik KS. (2001). Neuronal RNA granules: a link between RNA localization and stimulation-dependent translation. *Neuron* 32, 683-696.

Krogan, N.J., Kim, M., Tong, A., Golshani, A., Cagney, G., Canadien, V., Richards, D.P., Beattie, B.K., Emili, A., Boone, C., Shilatifard, A., Buratowski, S., and Greenblatt, J. (2003). Methylation of histone H3 by Set2 in *Saccharomyces cerevisiae* is linked to transcriptional elongation by RNA polymerase II. *Mol Cell Biol.* 23, 4207-4218.

Lai, M.C., Bechy, A.L., Denk, F., Collins, E., Gavrieliouk, M., Zaugg, J.B., Ryan, B.J., Wade-Martins, R., and Caffrey, T.M. (2017). Haplotype-specific MAPT exon 3 expression regulated by common intronic polymorphisms associated with Parkinsonian disorders. *Mol. Neurodegener.* 12, 79.

Lee, J.A., Damianov, A., Lin, C.H., Fontes, M., Parikshak, N.N., Anderson, E.S., Geschwind, D.H., Black, D.L., and Martin, K.C. (2016). Cytoplasmic Rbfox1 Regulates the Expression of Synaptic and Autism-Related Genes. *Neuron*.

Liu, B., Molinaro, G., Shu, H., Stackpole, E.E., Huber, K.M., and Richter, J.D. (2019). Optimization of ribosome profiling using low-input brain tissue from fragile X syndrome model mice. *Nucleic Acids Res.* 47, e25.

Liu, B., Li, Y., Stackpole, E.E., Novak, A., Gao, Y., Zhao, Y., Zhao, X., and Richter, J.D. (2018). Regulatory discrimination of mRNAs by FMRP controls mouse adult neural stem cell differentiation. *Proc. Natl. Acad. Sci. U.S.A.* *115*, E11397-E11405.

Lumish, H.S., Wynn, J., Devinsky, O., and Chung, W.K. (2015). Brief report: SETD2 mutation in a child with autism, intellectual disabilities and epilepsy. *J Autism Dev Disord.* *45*, 3764-3770.

Luo, Y., Shan, G., Guo, W., Smrt, R.D., Johnson, E.B., Li, X., Pfeiffer, R.L., Szulwach, K.E., Duan, R., Barkho, B.Z., Li, W., Liu, C., Jin, P., and Zhao, X. (2010). Fragile x mental retardation protein regulates proliferation and differentiation of adult neural stem/progenitor cells. *PLoS Genet.* *6*, e1000898.

Mallardo, M., Deitinghoff, A., Müller, J., Goetze, B., Macchi, P., Peters, C., and Kiebler, M.A. (2003). Isolation and characterization of Staufen-containing ribonucleoprotein particles from rat brain. *Proc Natl Acad Sci U S A.* *100*, 2100-2105.

McCamphill PK, Farah CA, Anadolu MN, Hoque S, Sossin WS. (2015). Bidirectional regulation of eEF2 phosphorylation controls synaptic plasticity by decoding neuronal activity patterns. *J Neurosci.* *35*, 4403-4417.

Maurin, T., Lebrigand, K., Castagnola, S., Paquet, A., Jarjat, M., Popa, A., Grossi, M., Rage, F., and Bardoni, B. (2018). HITS-CLIP in various brain areas reveals new targets and new modalities of RNA binding by fragile X mental retardation protein. *Nucleic Acids Res.* *46*, 6344-6355.

Neri, F., Rapelli, S., Krepelova, A., Incarnato, D., Parlato, C., Basile, G., Maldotti, M., Anselmi, F., and Olivero, S. (2017). Intragenic DNA methylation prevents spurious transcription initiation. *Nature* *543*, 72-77.

Parikshak, N.N., Swarup, V., Belgard, T.G., Irimia, M., Ramaswami, G., Gandal, M.J., Hartl, C.,

Leppa, V., Ubieta, L.D.L.T., Huang, J., et al. (2016). Genome-wide changes in lncRNA, splicing, and regional gene expression patterns in autism. *Nature*.

Quesnel-Vallières, M., Dargaei, Z., Irimia, M., Gonatopoulos-Pournatzis, T., Ip, J.Y., Wu, M., Sterne-Weiler, T., Nakagawa, S., Woodin, M.A., Blencowe, B.J., et al. (2016). Misregulation of an Activity-Dependent Splicing Network as a Common Mechanism Underlying Autism Spectrum Disorders. *Mol. Cell*.

Quesnel-Vallières, M., Weatheritt, R.J., Cordes, S.P., and Blencowe, B.J. (2019). Autism spectrum disorder: insights into convergent mechanisms from transcriptomics. *Nat Rev Genet.* *20*, 51-63.

Richter, J.D., Bassell, G.J., and Klann, E. (2015). Dysregulation and restoration of translational homeostasis in fragile X syndrome. *Nat. Rev. Neurosci.* *16*, 595-605.

Rockenstein, E.M., McConlogue, L., Tan, H., Power, M., Masliah, E., and Mucke, L. (1995). Levels and alternative splicing of amyloid β protein precursor (APP) transcripts in brains of APP transgenic mice and humans with Alzheimer's disease. *J. Biol. Chem.* *270*, 28257-28267.

Santoro, M.R., Bray, S.M., and Warren, S.T. (2012). Molecular mechanisms of fragile X syndrome: a twenty-year perspective. *Annu. Rev. Pathol.* *7*, 219-245.

Scheetz AJ, Nairn AC, Constantine-Paton M. (2000). NMDA receptor-mediated control of protein synthesis at developing synapses. *Nat Neurosci.* *3*, 211-216.

Schuller AP, Wu CC, Dever TE, Buskirk AR, Green R. (2017). eIF5A Functions Globally in Translation Elongation and Termination. *Mol Cell.* *66*, 194-205.

Shen, S., Park, J.W., Lu, Z., Lin, L., Henry, M.D., Wu, Y.N., Zhou, Q., and Xing, Y. (2014). rMATS:

Robust and flexible detection of differential alternative splicing from replicate RNA-Seq data. *Proc. Natl. Acad. Sci.* *111*, E5593-E5601.

Stefani, G., Fraser, C.E., Darnell, J.C., and Darnell, R.B. (2004). Fragile X mental retardation protein is associated with translating polyribosomes in neuronal cells. *J. Neurosci.* *24*, 7272-7276.

Sutton MA, Taylor AM, Ito HT, Pham A, Schuman EM. (2007). Postsynaptic decoding of neural activity: eEF2 as a biochemical sensor coupling miniature synaptic transmission to local protein synthesis. *Neuron* *55*, 648-661.

Tabet, R., Moutin, E., Becker, J.A., Heintz, D., Fouillen, L., Flatter, E., Krężel, W., Alunni, V., Koebel, P., Dembélé, D., Tassone, F., Bardoni, B., Mandel, J.L., Vitale, N., Muller, D., Le Merrer, J., and Moine, H. (2016). Fragile X Mental Retardation Protein (FMRP) controls diacylglycerol kinase activity in neurons. *Proc. Natl. Acad. Sci. U.S.A.* *113*, E3619-3628.

Thomson, S.R, Seo, S.S., Barnes, S.A., Louros, S.R., Muscas, M., Dando, O., Kirby, C., Wyllie, D.J.A., Hardingham, G.E., Kind, P.C., and Osterweil, E.K. (2017). Cell-type-specific translation profiling reveals a novel strategy for treating fragile X syndrome. *Neuron* *95*, 550-563.

Tiedemann, R.L., Hlady, R.A., Hanavan, P.D., Lake, D.F., Tibes, R., Lee, J.H., Choi, J.H., Ho, T.H., and Robertson, K.D. (2016). Dynamic reprogramming of DNA methylation in SETD2-deregulated renal cell carcinoma. *Oncotarget* *7*, 1927-1946.

Udagawa, T., Farny, N.G., Jakovcevski, M., Kaphzan, H., Alarcon, J.M., Anilkumar, S., Ivshina, M., Hurt, J.A., Nagaoka, K., Nalavadi, V.C., Lorenz, L.J., Bassell, G.J., Akbarian, S., Chattarji, S., Klann, E., and Richter, J.D. (2013). Genetic and acute CPEB1 depletion ameliorate fragile X pathophysiology. *Nat. Med.* *19*, 1473-1477.

Van Bokhoven, H. (2011). Genetic and epigenetic networks in intellectual disabilities. *Ann. Rev. Genet.* *48*, 81-104.

Ward Jr, J.H. (1963). Hierarchical grouping to optimize an objective function. *J. Amer. Statistical Assoc.* *58*, 236-244.

Wang, C.X., Cui, G.S., Liu, X., Xu, K., Wang, M., Zhang, X.X., Jiang, L.Y., Li, A., Yang, Y., Lai, W.Y., et al. (2018). METTL3-mediated m⁶A modification is required for cerebellar development. *PLoS Biol.* *16*, e2004880.

Waung, M.W., and Huber, K.M. (2009). Protein translation in synaptic plasticity: mGluR-LTD, Fragile X. *Curr. Opin. Neurobiol.* *19*, 319-326.

Xu, S., Grullon, S., Ge, K., and Peng, W. (2014). Spatial clustering for identification of chip-enriched regions (SICER) to map regions of histone methylation patterns in embryonic stem cells. *Methods Mol. Biol.* *1150*, 97-111.

Xu, Y., Zhao, W., Olson, S.D., Prabhakara, K.S., and Zhou, X. (2018). Alternative splicing links histone modifications to stem cell fate decision. *Genome Biol.* *19*, 133.

Yu, G., Wang, L.-G., Han, Y., and He, Q.-Y. (2012). clusterProfiler: an R package for comparing biological themes among gene clusters. *Omic: a journal of integrative biology* *16*, 284-287.

Yukselen, O., Turkyilmaz, O., Ozturk, A., Garber, M., and Kucukural, A. (2019). DolphinNext: A distributed data processing platform for high throughput genomics. *BioRxiv*.

Figure Legends

Figure 1. Ribosome Profiling Reveals Diverse Changes of Gene Expression in *Fmr1* KO Hippocampus.

(A) Schematic diagram of the hippocampal slice preparation. To reduce spontaneous electrical activity, region CA3 was excised.

(B) Schematic diagram of the experimental procedures for ribosome profiling.

(C) Scatter plot of expression changes of mRNA levels and ribosome protected fragments (RPFs). Dysregulated mRNAs in the absence of FMRP are classified into four regulatory groups. 14459 genes past filtering are used for the scatter plot. Nominal p-value < 0.01, FDR = 0.097 by permutation test. FC, fold change. TE, translational efficiency.

(D) Top 3 GO terms of Biological Process enriched in each regulatory group. The enrichment (gene ratio) is represented by the size of dots. The enrichment significance (adjusted p-value) is color coded.

(E) Top 3 GO terms of Cellular Component enriched in each regulatory group. (also see Figure S1, Table S1)

Figure 2. Characterization of Genes with Translational Efficiency Changes in *Fmr1* KO Hippocampus.

(A) Heatmap of expression changes (\log_2 FC KO/WT) for the top 20 RNAs in the “TE up” group.

(B) Heatmap of expression changes (\log_2 FC KO/WT) for the top 20 RNAs in the “TE down” group.

(C) Read distributions on the *Gfpt2* RNA of TE up group. FMRP CLIP tags (top) (Darnell et al 2011), normalized RPF reads (middle), and mRNA reads (bottom) averaged across all replicates are plotted along the mRNA nucleotide positions with green and red triangles for annotated start and stop codons respectively. For visualization purposes, the curves were smoothed within a 30nt window.

(D) Read distributions on the *Lhfpl2* RNA of TE down group.

(E) Boxplots visualize the medians of expression changes for FMRP CLIP targets. The lower and upper hinges correspond to the first and third quartiles. The whiskers extend from the hinges to the largest and smallest values no further than 1.5 fold of inter-quartile range. Outliers are not shown. Gene expression changes of CLIP genes were compared to those of all genes used for DEG analysis (ns: not significant, **** p-value <0.0001, Wilcoxon rank sum test after multiple test correction with the Bonferroni method). CLIP genes are the FMRP targets identified in (Darnell et al 2011).

(F) Overlap of the TE down and up genes detected in this study (orange) with those of Das Sharma et al (2019 (green) and the TRAP-seq data of Thomson et al (2017) (blue).

(G) Schematic models of ribosome density (TE) changes that reflect increased protein synthesis rates. (also see Table S1)

Figure 3. Run-off ribosome profiling of WT mouse brain slices.

(A) Schematic diagram of homoharringtonine (HHT) run-off ribosome profiling. WT mouse brain splices was treated with 20 μ M HHT, an inhibitor of translation initiation, to allow ribosome run-off for 5, 10, 30, and 60min (t) at 30°C.

(B) Metagene plot of RPFs after HHT treatment. Reads are mapped transcripts (N=1401) with CDS longer than 3000nt, and aligned at the annotated start and stop codons (grey vertical dash lines). The read densities at each nucleotide position are normalized to the average density of the last 500nt of CDS and averaged using the P sites of RPFs. For visualization purposes, the curves were smoothed within a 90nt window. Black horizontal dash line indicates the arbitrary 0.8 threshold to estimate the relative run-off distances (black vertical dash lines).

(C) Linear regression between the HHT treatment time and ribosome run-off distances (from B) to estimate the global elongation rate (4.2 nt/sec).

- (D) Cluster analysis of gene groups with distinct ribosome run-off patterns. The RPFs of each gene at each time point was formalized to time 0. The Euclidean distance matrix was then calculated, followed by hierarchical clustering using Ward's agglomeration method (Ward, 1963).
- (E) Ribosome runoff patterns for each sub-cluster. The global pattern of each sub-cluster was summarized using the corresponding median and standard deviation in each timepoint. The number of RNAs in each sub-cluster is shown in parentheses.
- (F) Representative ribosome runoff profiles that reflect each sub-cluster. The runoff pattern for *Actin* is similar to sub-clusters 4-6.
- (G) Ribosome footprints for *Nrxn3* and *Actin* mRNAs during the runoff time period.
- (H) GO terms for sub-clusters 1 and 3. Gene ratio refers to the percentage of total differentially expressed genes in the given GO term. (also see Figure S2, Table S1)

Figure 4. Substantial FMRP remains associated with polysomes after HHT treatment.

- (A-D) WT mouse hippocampal slices were treated with DMSO vehicle (A) or 20 μ M HHT (B) for 30min at 30°C. In parallel, *Fmr1* KO mouse hippocampal slices were also treated with DMSO vehicle (C) or 20 μ M HHT (D) for 30min at 30°C. Slices were homogenized and applied to 15-45% (w/w) sucrose gradients, which were fractionated with continuous monitoring of A_{260} after the ultracentrifugation. Fractions were collected for immunoblotting with indicated antibodies to detect the association of FMRP with polysomes.
- (E) RNA sedimenting to “heavy” fractions containing >7 ribosomes from WT slices treated with HHT was analyzed relative to input. 1574 RNAs were reduced and 686 were elevated relative to input after HHT treatment.
- (F) *Actin* mRNA reads in the designated conditions (WT, wild type; V, vehicle, I, input; H, heavy fractions, KO, *Fmr1* KO).
- (G) *Map 1b* mRNA reads in the designated conditions.
- (H) GO terms of RNAs depleted in heavy fractions relative to WT.

(I) GO terms of RNAs enriched in heavy fractions relative to WT. (also see Figure S3, Table S1)

Figure 5. FMRP stalls ribosomes on specific mRNAs.

(A) RNA sedimenting to “medium” polysomes containing 4-6 ribosomes after HHT treatment of hippocampal slices; 46 RNAs are down-regulated and 1 is up-regulated in *Fmr1* KO relative to WT.

(B) Down-regulated RNAs in HHT-treated *Fmr1* KO slices primarily encode epigenetic and transcriptional regulators and proteins involved in neural function.

(C) Example of *Ankrd12* RNA, which has reduced reads in *Fmr1* KO slices relative to WT after HHT (H) treatment. Input (I) reads are similar in both genotypes. M refers to medium fraction.

(D) Box plot showing the fold change of *Fmr1* KO versus WT of all RNAs (white) compared to those identified in Figure 5 A and B (gray) with respect to steady state RNA levels, RPFs, and TE (ns: not significant, *p-value <0.01, **p-value <0.001, Wilcoxon rank sum test after multiple test correction with the Bonferroni method).

(E) Western analysis of SETD2 and lamin ac in hippocampus from 4 WT and 5 *Fmr1* KO mice. When quantified and made relative to Lamin AC, SETD2 was significantly increased in the KO (p=0.0245, two-tailed t test). (also see Table S1)

Figure 6. H3K36me3 localization is altered in *Fmr1* KO hippocampus.

(A) Experimental design for *in vivo* ChIP-seq of H3K36me3 in hippocampus from adult WT (N=4) and *Fmr1* KO (N=4) mice.

(B. I) Pie chart representing the genomic annotation of the total H3K36me3 islands identified in the WT and *Fmr1* KO ChIP-seq. II) Venn diagram illustrating the number of genes with H3K36me3 islands identified in WT (blue) and *Fmr1* KO (green) ChIP-seq in both biological replicates combined.

(C) H3K36me3 ChIP-seq gene tracks for WT and *Fmr1* KO hippocampal tissue. The two sequencing tracks from each biological replicate (n=2) of WT and *Fmr1* KO were merged and overlaid. WT ChIP-seq tracks are in blue and KO tracks are in green. The tracks for IP and input are displayed. The island with significantly decreased (blue) or increased (green) tracks are shown below the Refseq gene annotation (FDR <0.0001 and p-value <0.01) as identified using the SICER package. *Reep4* shows decreased H3K36me3 islands in *Fmr1* KO and *Tprkb* shows increased islands in *Fmr1* KO

(D) Distribution of significantly increased or decreased H3K36me3 islands as identified by SICER-df.sh package (FDR<0.0001 and p-value <0.0001) within genes (intragenic) or in gene proximal (intergenic) regions. The total number of increased or decreased islands is indicated above the respective bars in the graph in *Fmr1* KO vs wild type ChIP-seq.

(E) Venn diagram for significant overlap of *Fmr1* KO mis-regulated H3K36me3 genes (increased islands in green and decreased islands in blue) with the ASD-linked genes from the SFARI database. A subset of genes (219) showed both increased and decreased islands along the length of the gene body. The p-value is indicated next to the respective comparisons.

(F) GO term enrichment of H3K36me3 differentially enriched genes in *Fmr1* KO vs WT (p.adjust value<0.05). (also see Figure S4, Table S2)

Figure 7. Global analysis of FMRP mediated alternative splicing (AS).

(A) Summary table of total splicing events in *Fmr1* KO and WT based on RNA-seq from hippocampal slices. Splicing events detected by rMATS at a FDR < 5% and a difference in the exon inclusion levels between the genotypes ($\Delta\text{PSI} \geq 5\%$) are depicted.

(B) Alternatively spliced events validated using RT-qPCR are shown for several RNAs (hippocampus tissue, WT, n=6; *Fmr1* KO, n=6). The illustration depicts an example of exon skipping (green box) in the *Fmr1* KO. Primer positions are depicted with black bars.

(C) Alternative splicing events detected in *Fmr1* KO and WT hippocampus. Inclusion events that were significantly (p -value <0.05) increased (red), decreased (blue), or unchanged (gray) are indicated. The number of events in the up or down category are shown in red and blue, respectively. PSI, (Percent Splice In / Exon inclusion levels).

(D) GO term enrichment for all alternative splicing events are shown (p .adjust value <0.05). The total number of genes identified in the RNA-seq from (Figure 1) were used as background.

(E) Table depicting the overlap of the alternatively spliced (Alt. Spl./AS) genes in this study with the SFARI Autism Spectrum Disorder database, the Alt. Spl. genes identified in samples from autism patients (Parikshak et al., 2016), and genes with increased or decreased H3K36me3 islands from Figure 6. The intensity of the color represents the increasing number of overlapping genes between the gene sets. Asterisks indicate statistical significance.

(F) Violin plot for the H3K36me3 ChIP signal at the 5' (SS5) and 3' (SS3) splice sites of the alternatively skipped exons in WT (white) and *Fmr1* KO (red) hippocampus tissue (p -value <0.05 , KS test for significance).

(G) Model for FMRP mediated alterations in H3K36me3 marks on the chromatin and alternative splicing of transcripts in the hippocampus. (also see Table S3)

Figure S1. Clustering of RNAs with changes in TE and mRNA abundance to identify functional hubs (Related to Figure 1, also see TableS1)

(A) Network clustering of “mRNA up” RNAs from the ribosome profiling and RNA-seq in WT and *Fmr1* KO hippocampus. Nodes indicate the functional processes linked to the RNAs identified. Fold changes are indicated.

(B) Network clustering of the functional processes in the “mRNA down” RNAs

(C) Network analysis of the of the functional processes in the “TE down” mRNAs

Figure S2. Run-off ribosome profiling of WT mouse hippocampal slices. (Related to Figure 3, also see Table S1)

(A) Ribosome runoff patterns for clusters 1 and 2. The RPFs of each gene at each time point was normalized to time 0. The euclidean distance matrix was then calculated, followed by hierarchical clustering using Ward's agglomeration method (Ward, 1963). The global pattern of each sub-cluster was summarized using the corresponding median and standard deviation in each timepoint. Representative ribosome runoff profiles are shown.

(B) CDS length dependency of the ribosome runoff rates. Results of the KS test for significance are shown

(C) GO terms for sub-clusters 2,4, 5 and 6.

Figure S3. Sedimentation of proteins in polysome sucrose gradients. (Related to Figure 4, also see Table S1)

(A) Hippocampal extracts, some of which were treated with RNAse A, were centrifuged through sucrose gradients, fractionated, and immunoblotted for FMRP, RPS6 and RPL4. Long and short refer to relative exposure times.

(B) Hippocampal slices from WT or FMRP KO mice were treated with vehicle only or HHT for 30 min. The gradients were fractionated and immunoblotted for the indicated proteins. The red arrow denotes the eEF2 band. The medium polysome fractions are indicated.

Figure S4. H3K36me3 ChIP metagene analysis (Related to Figure 6, also see Table S2)

(A) Scatter plot for ChIP-seq normalized reads density (Transcripts per million mapped reads, TPM) mapped to the genic regions between biological replicate samples, WT1 and WT2 and *Fmr1* KO1 and *Fmr1* KO2. r values for correlation efficiency is shown. Asterisks indicate statistical significance.

(B) Metagene plots using deepTools for distribution of H3K36me3 marks along the gene lengths.

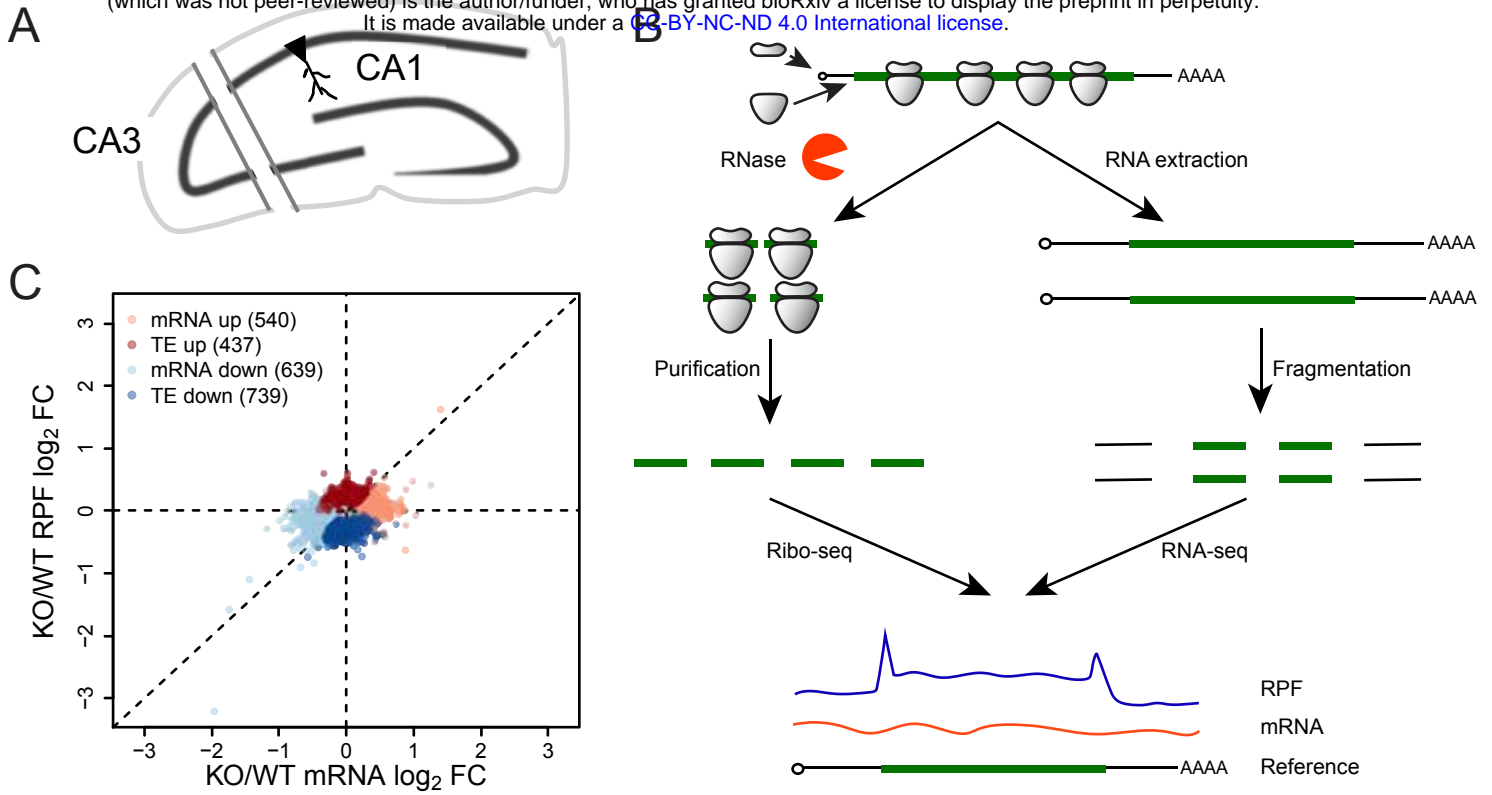
A similar increase in ChIP signal in all samples is seen in the gene body. The transcription start site (TSS), Transcription end site (TES) and 2.0kb downstream is shown.

(C) Heatmap for distribution of H3K36me3 signal along the gene length in each sample, compiled plot in Figure S4B. The transcription start site (TSS), Transcription end site (TES) and 4.0kb downstream is shown. No overall differences in ChIP signal was observed between samples.

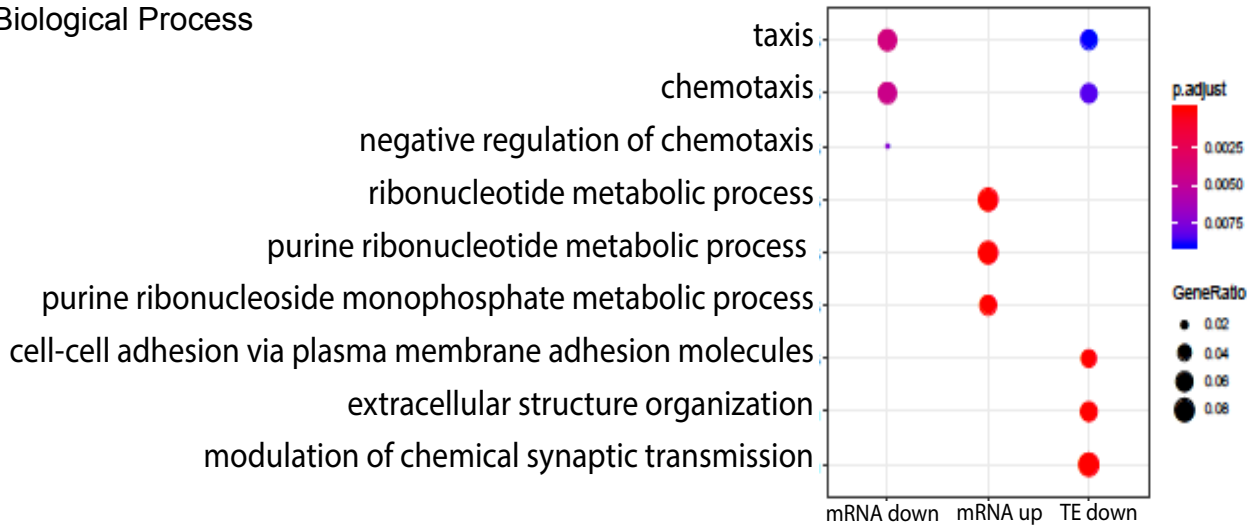
(D) Violin plot to assess the effect of gene length on H3K36me3 ChIP signal between WT (white) and *Fmr1* KO (red) samples.

(E) Histogram depicting number of islands (log scale) and their respective island length for all significant islands (bp in log scale) identified in the WT (blue) and *Fmr1* KO (green) ChIP-seq. The island lengths were parsed in bins of 100bp and the center of each bin is plotted in the histogram. Asterisks indicate statistical significance.

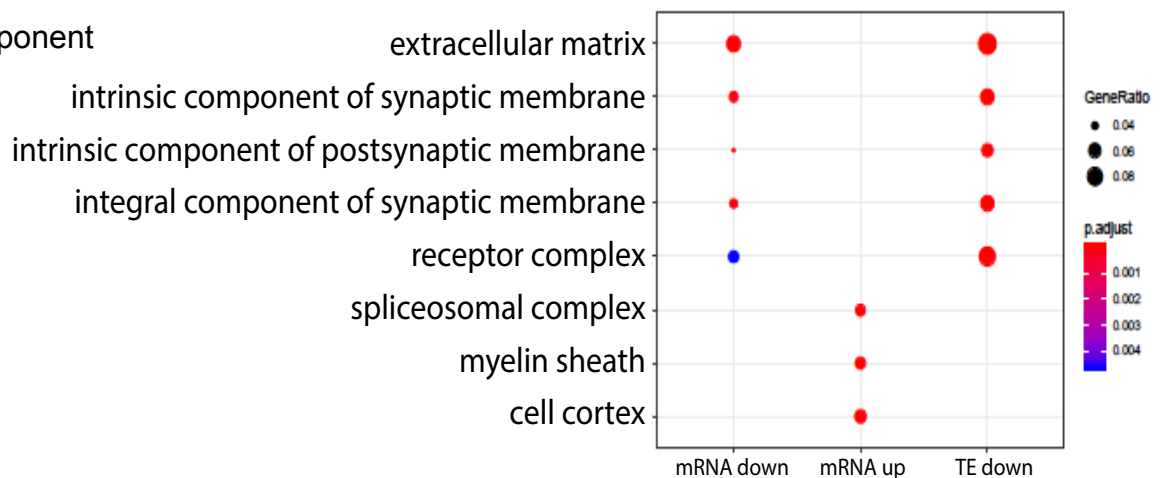
bioRxiv preprint first posted online Oct. 10, 2019; doi: <http://dx.doi.org/10.1101/801076>. The copyright holder for this preprint (which was not peer-reviewed) is the author/funder, who has granted bioRxiv a license to display the preprint in perpetuity. It is made available under a [CC-BY-NC-ND 4.0 International license](https://creativecommons.org/licenses/by-nc-nd/4.0/).



D Biological Process



E Cellular component



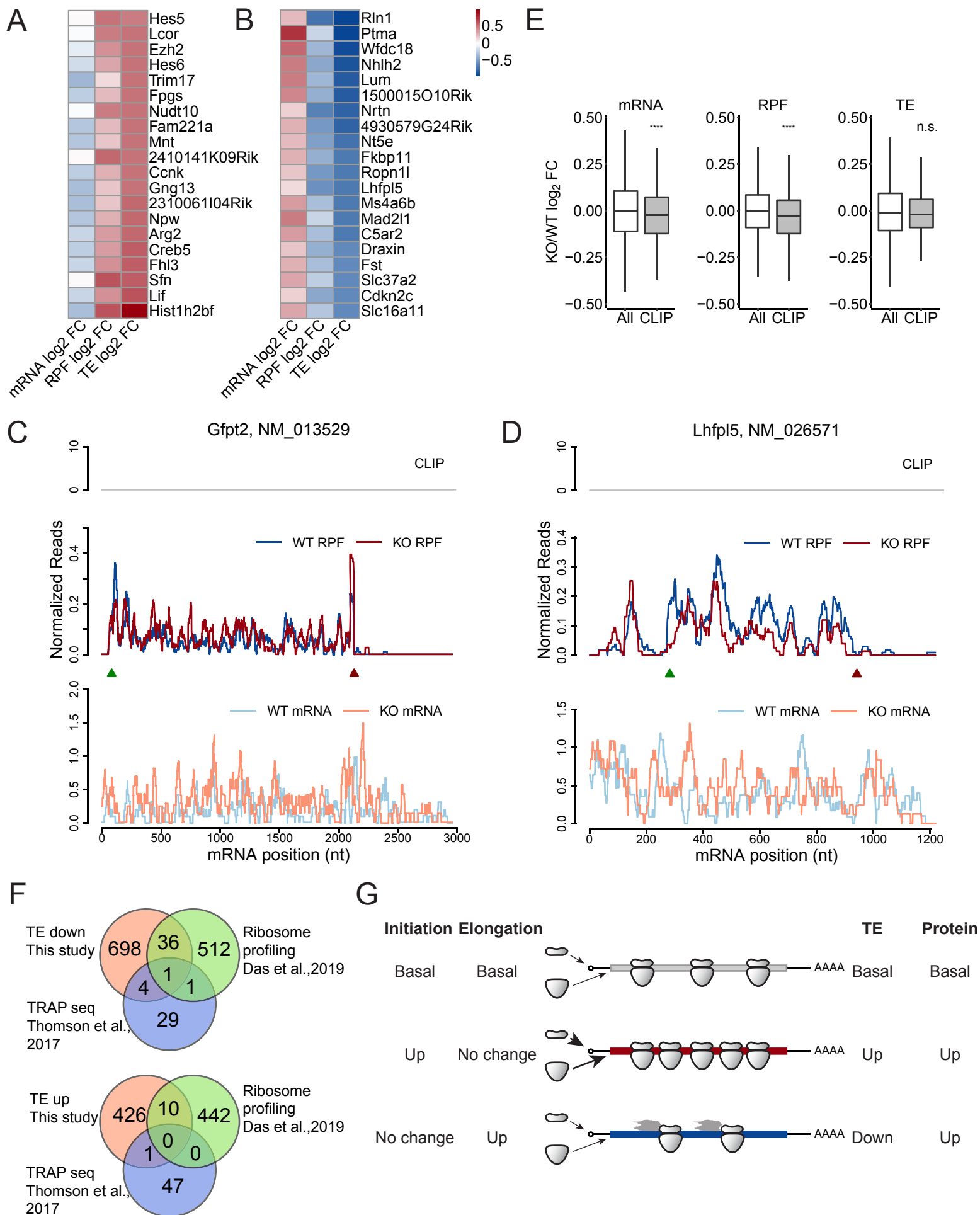
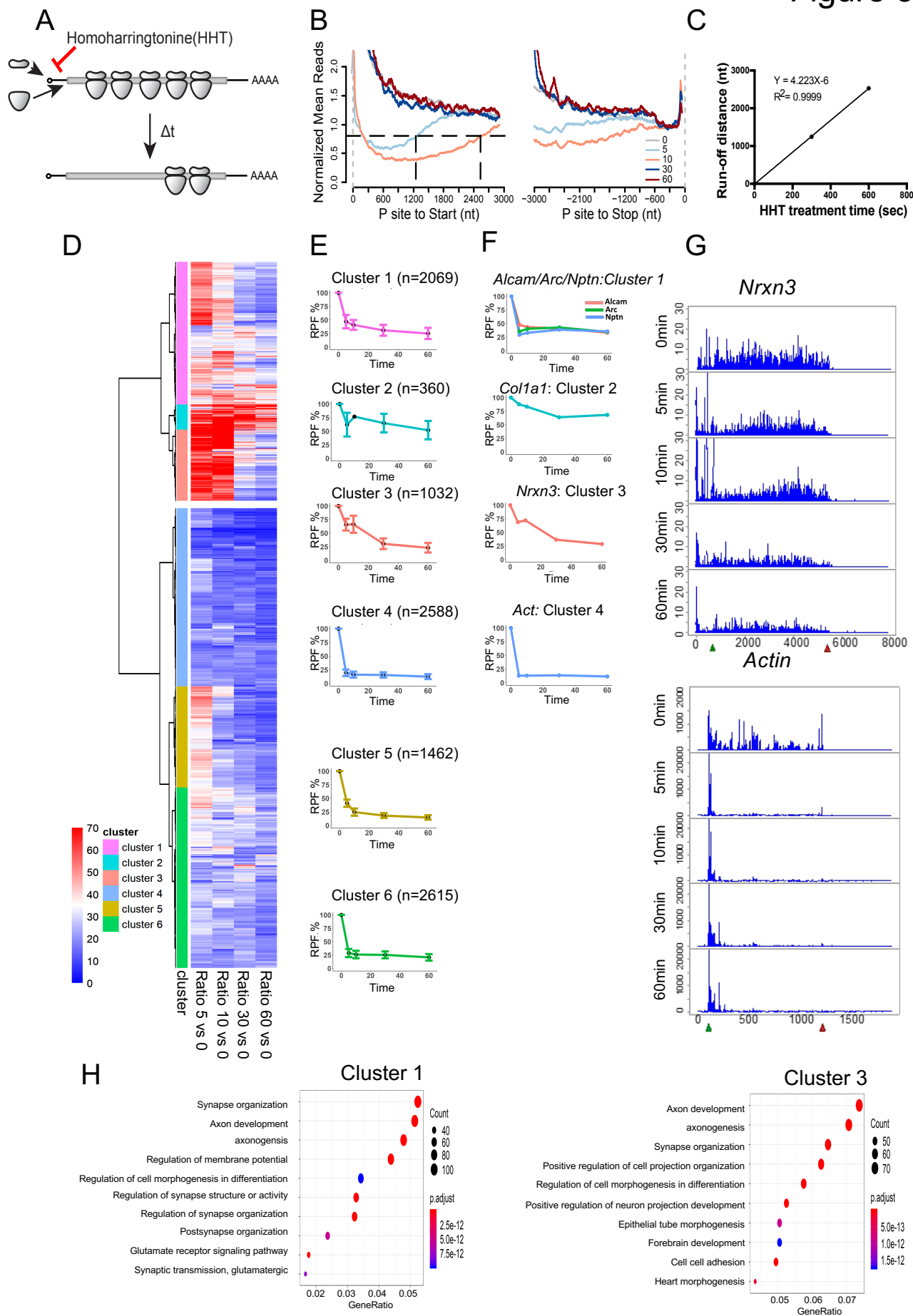
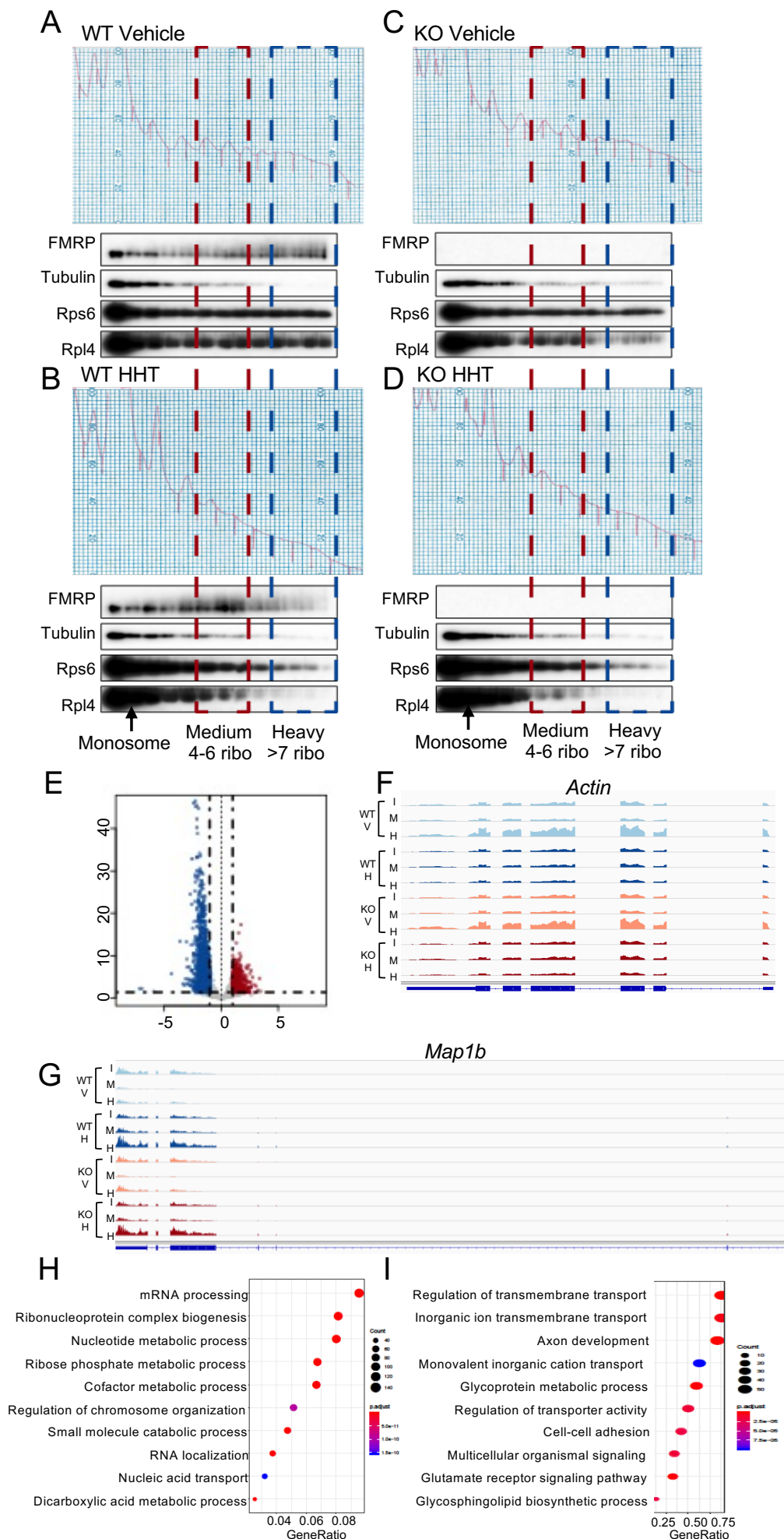


Figure 3





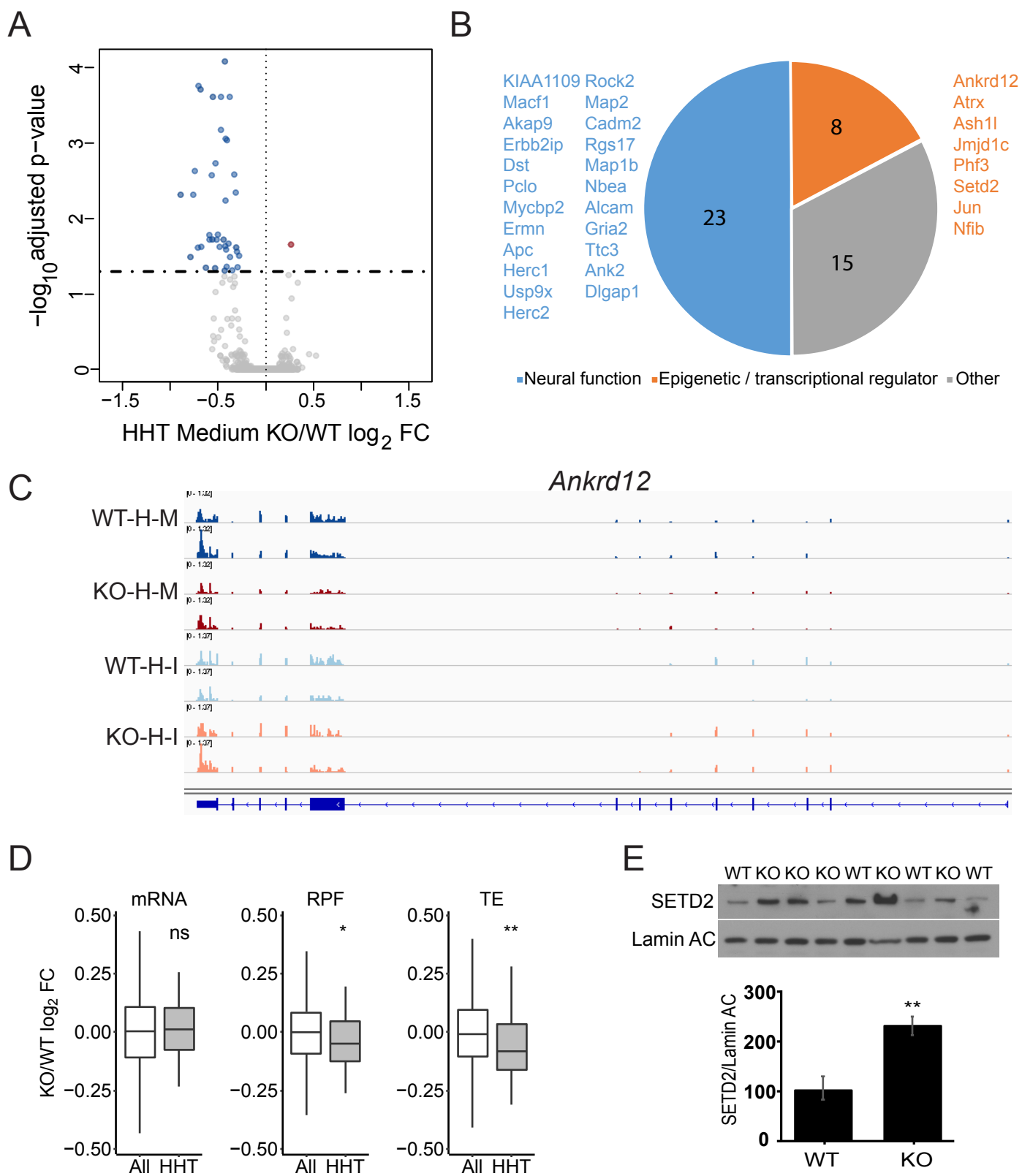


Figure 6

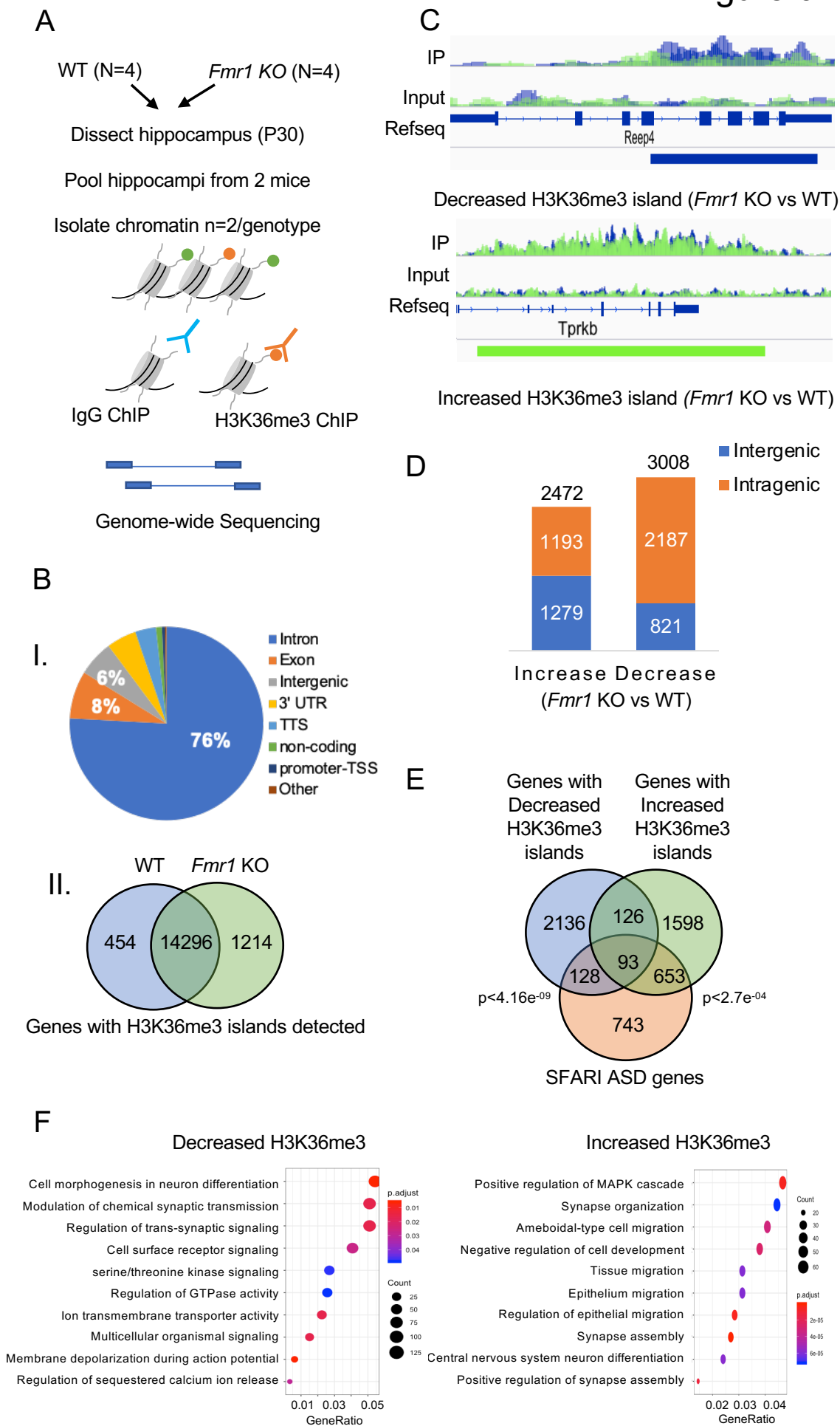


Figure 7

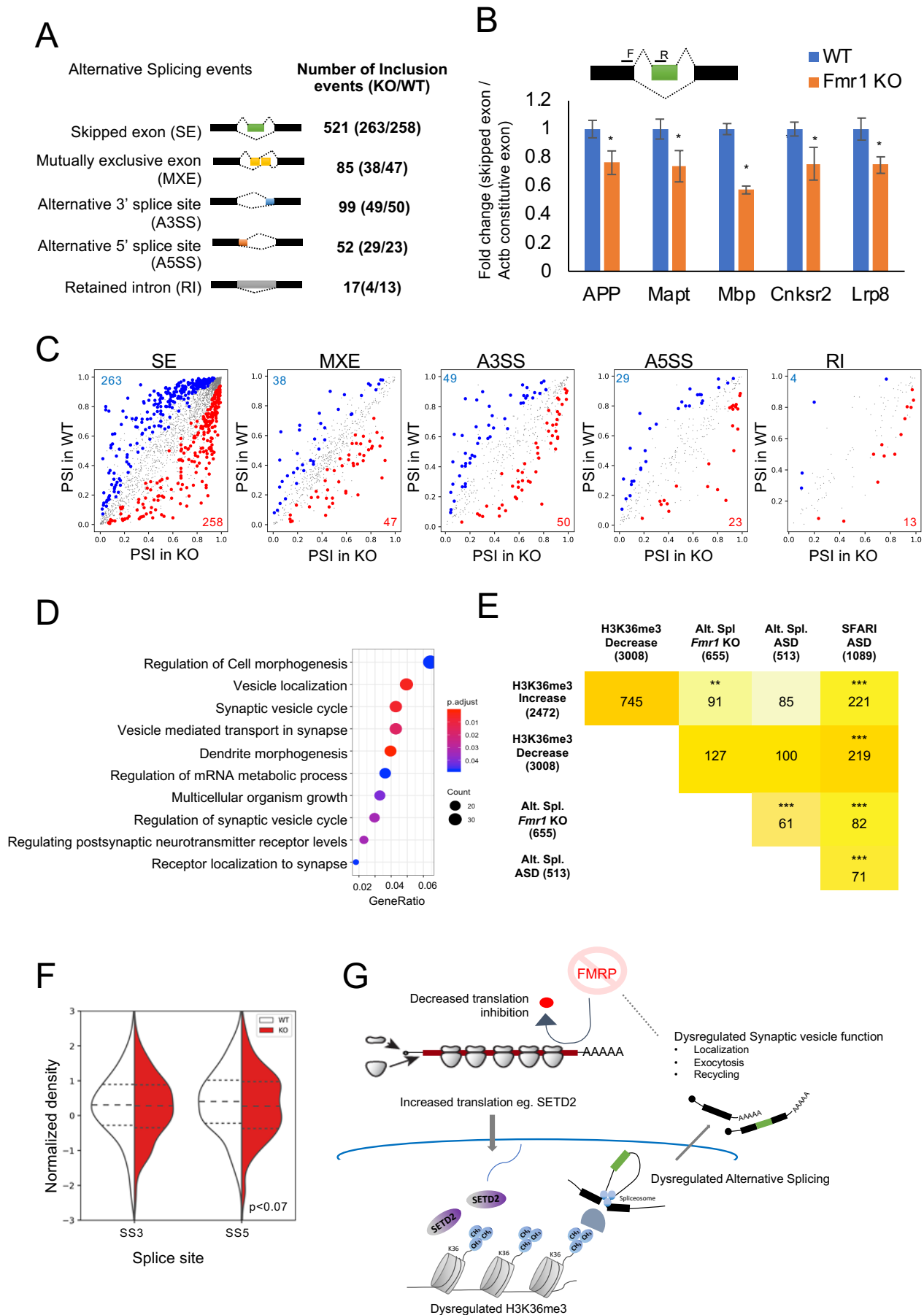


Figure S1

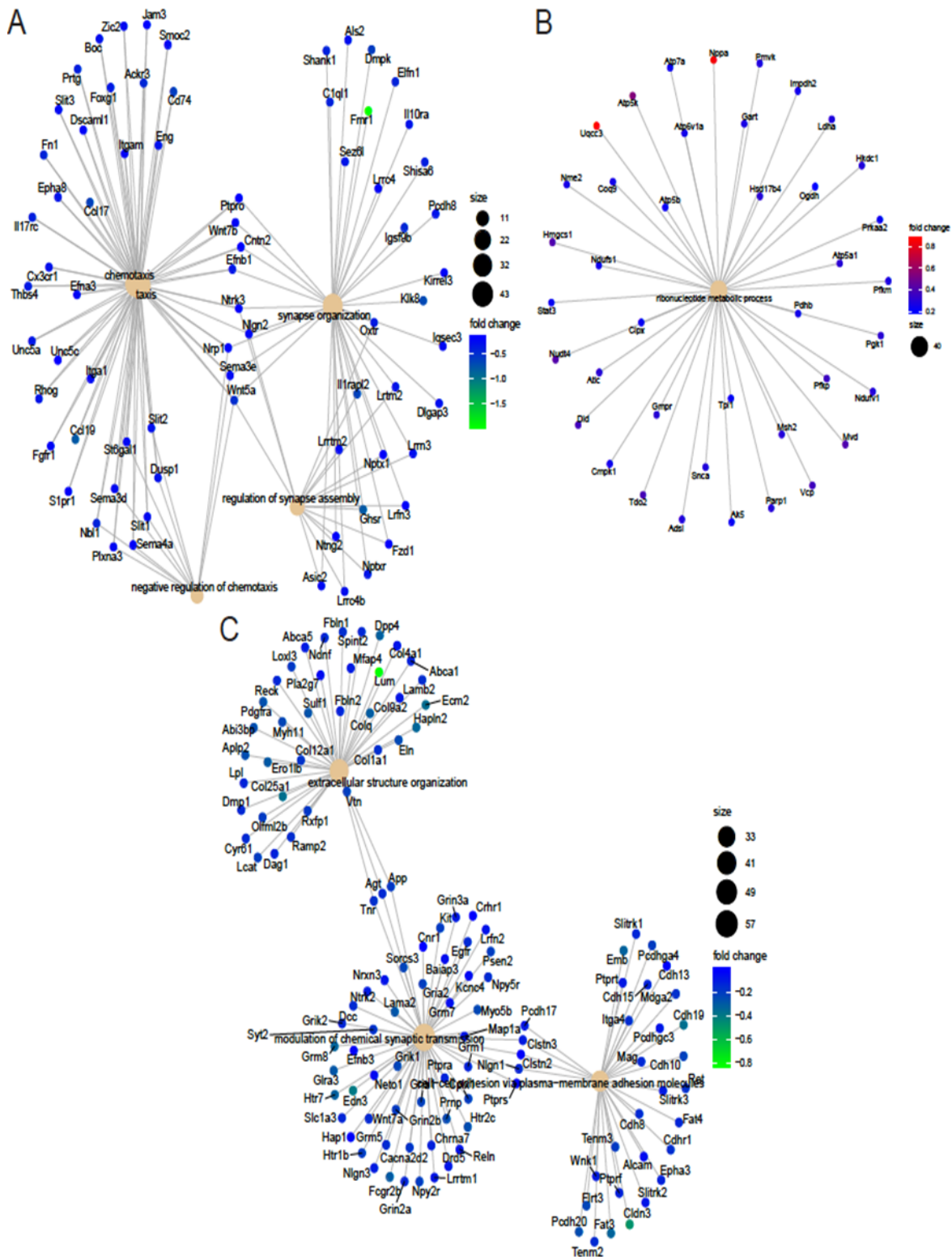


Figure S2

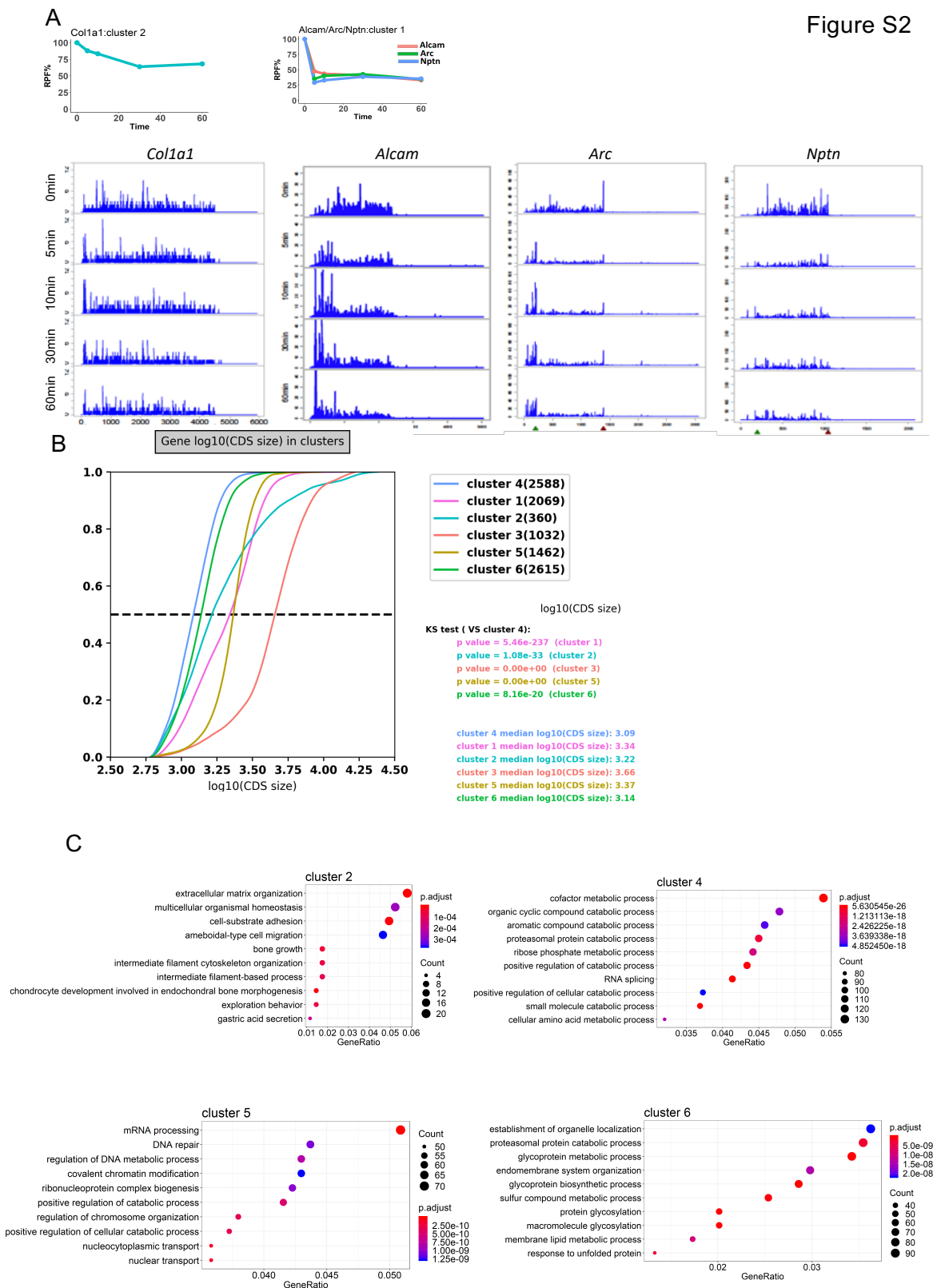
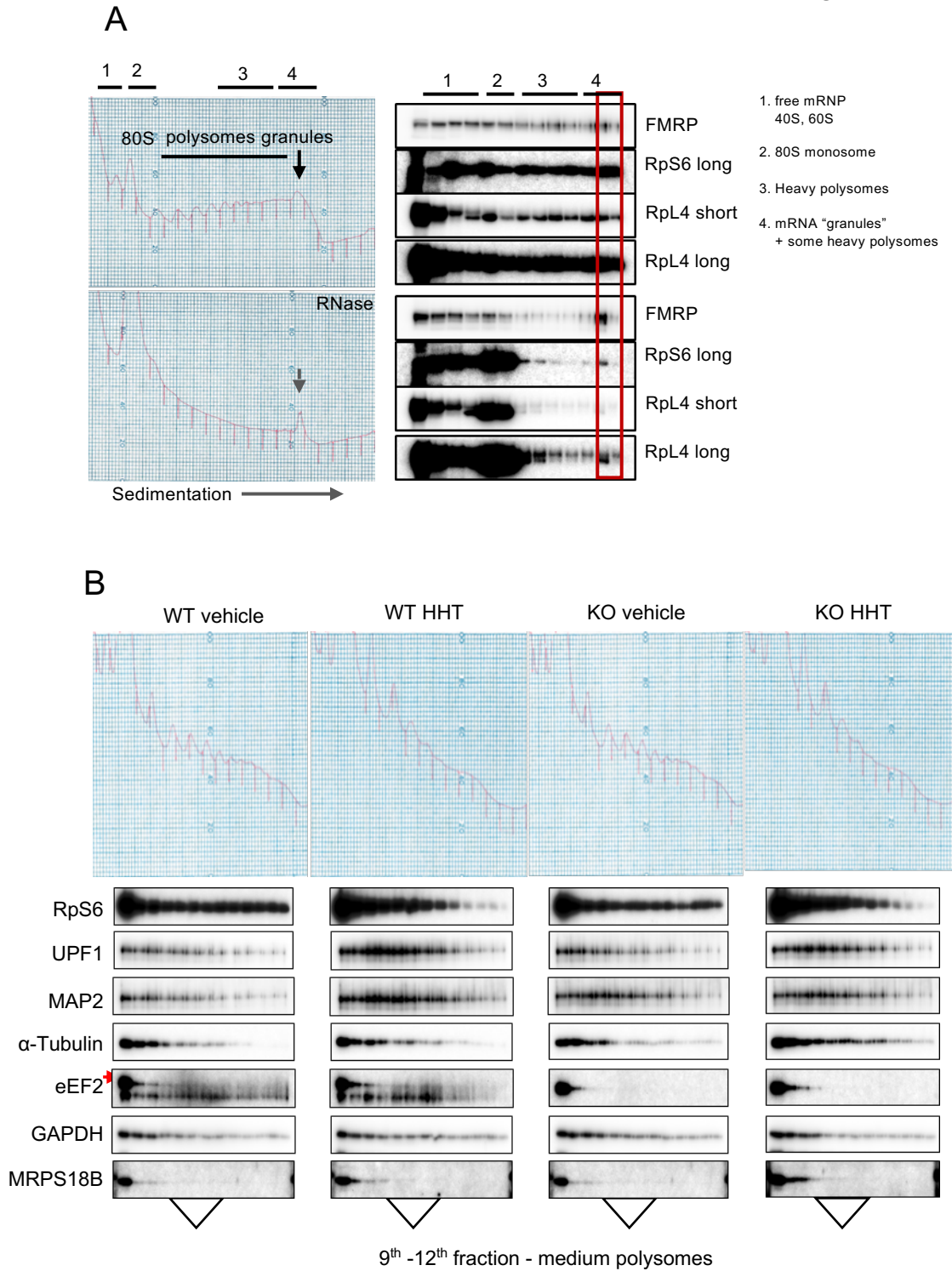
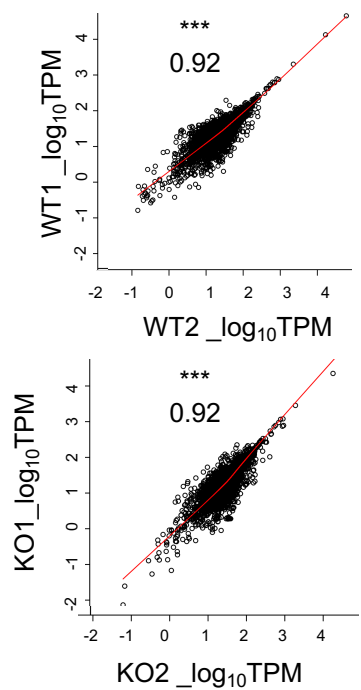


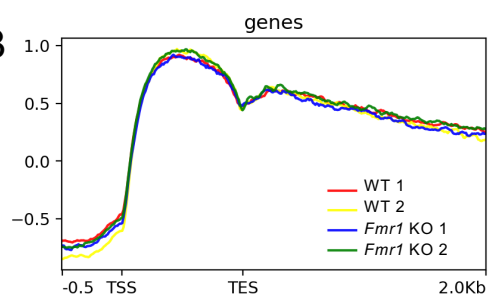
Figure S3



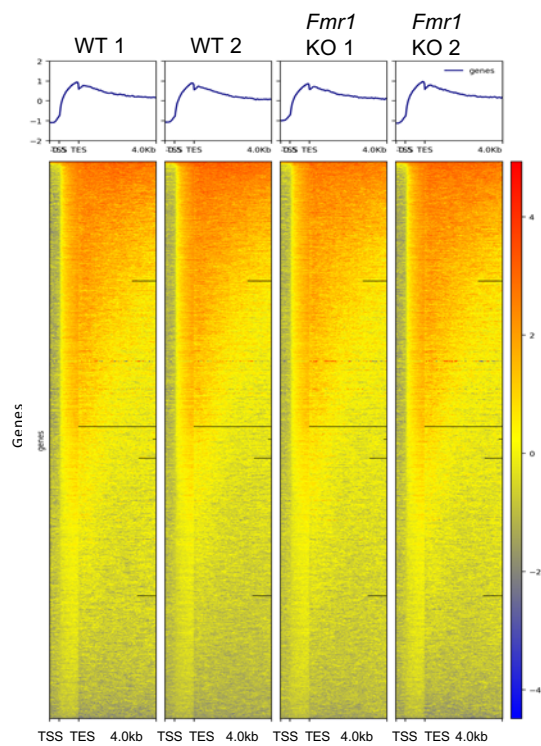
A



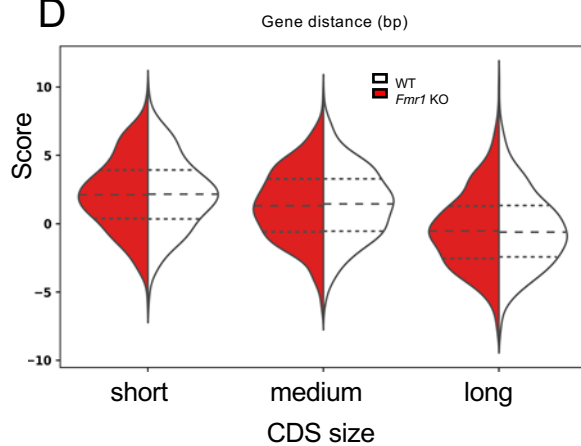
B



C



D



E

